CZECH TECHNICAL UNIVERSITY IN PRAGUE

Faculty of Mechanical Engineering

Department of Mechanics, Biomechanics and Mechatronics

ANISOTROPY INFLUENCE ON SHEET METAL PART FATIGUE LIFE

Martin Jakubec

A thesis submitted for the degree of
Master of Science

2022

ZADÁNÍ DIPLOMOVÉ PRÁCE

I. OSOBNÍ A STUDIJNÍ ÚDAJE

Příjmení:	**Jakubec**	Jméno: **Martin**	Osobní číslo: **466547**

Fakulta/ústav: **Fakulta strojní**

Zadávající katedra/ústav: **Ústav mechaniky, biomechaniky a mechatroniky**

Studijní program: **Aplikované vědy ve strojním inženýrství**

Specializace: **Aplikovaná mechanika**

II. ÚDAJE K DIPLOMOVÉ PRÁCI

Název diplomové práce:

Vliv anisotropie na výpočet životnosti součásti vyrobené z plechu.

Název diplomové práce anglicky:

Anisotropy influence on the part manufactred of sheet metal life prediction.

Pokyny pro vypracování:

- Seznamte se s formulací a vlastnostmi fenomenologických modelů anisotropní plasticity implementovaných v MKP programu Ansys.
- Pro zadanou součást získejte potřebná experimentální data (od partnerské instituce nebo vlastním měřením) a identifikujte parametry zvoleného modelu anisotropní a standardního modelu isotropní plasticity.
- Vytvořte strukturovaný MKP model pro simulaci výrobního procesu zadané součásti a analýzu jejího zadaného provozního namáhání. Simulaci i analýzu proveďte pro oba identifikované modely plasticity a stanovte životnost při zadaném provozním cyklu pro oba modely.
- Formulujte závěry
-

Seznam doporučené literatury:

[1] Banabic, D. Sheet Metal Forming Processes, Constitutive Modelling and Numerical Simulation. Springer-Verlag Berlin and Heidelberg GmbH & Co. KG, 2010.I SBN 783540881124
[2] Crisfield, M.A. Non☐Linear Finite Element Analysis of Solids and Structures. John Wiley &Sons (October 9, 1996).
[3] Marciniak, Z. Duncan, J.L. Hu, S.J. Mechanics of Sheet Metal Forming. Elsevier Ltd., 2002
[3] Ansys Mechanical APDL Theory reference

Jméno a pracoviště vedoucí(ho) diplomové práce:

doc. Ing. Miroslav Španiel, CSc.   odbor pružnosti a pevnosti FS

Jméno a pracoviště druhé(ho) vedoucí(ho) nebo konzultanta(ky) diplomové práce:

Datum zadání diplomové práce: **12.04.2022**	Termín odevzdání diplomové práce: **14.08.2022**

Platnost zadání diplomové práce: _____

doc. Ing. Miroslav Španiel, CSc.	doc. Ing. Miroslav Španiel, CSc.	doc. Ing. Miroslav Španiel, CSc.
podpis vedoucí(ho) práce	podpis vedoucí(ho) ústavu/katedry	podpis děkana(ky)

III. PŘEVZETÍ ZADÁNÍ

Diplomant bere na vědomí, že je povinen vypracovat diplomovou práci samostatně, bez cizí pomoci, s výjimkou poskytnutých konzultací. Seznam použité literatury, jiných pramenů a jmen konzultantů je třeba uvést v diplomové práci.

28.4.2022	
Datum převzetí zadání	Podpis studenta

Abstract

The aim of this thesis is to evaluate the influence anisotropy has on a fatigue life of a anti-roll bar clamp made out of S420MC sheet metal. First, a brief overview theory of linear elasticity, anisotropic and isotropic models and commonly used parameters used to determine anisotropy influence are presented. After that, a material model using Hill's 1948 yield criterion is created and it's validity verified by simulating the uniaxial tensile and stack tests. The last part concerns with forming simulation in multiple directions, creating and verifying a hyperelastic material model for an elastomer rubber bearing through which the clamp is loaded and a press-fit simulation of this bearing into the clamp as well as its subsequent loading. Lastly a fatigue life calculation is done using the now known plastic strains from forming simulations and stress distributions from one load cycle.

Keywords

Anisotropy, Sheet metal, Forming, Plasticity, Fatigue life, Finite element analysis

Abstrakt

Cílem této diplomové práce je zhodnotit vliv anisotropie na životnostní vlastnosti svorky zkrutného stabilizátoru vyrobené z plechu S420MC. Nejprve je představena teorie lineární elasticity, anisotropní a isotropní modely a parametry používané k popisu anisotropního chování plechu. Dále je z experimentálně naměřených dat vytvořen materiálový model pomocí Hillovy teorie plasticity a ověřena správnost tohoto modelu pomocí simulace tahových a tlakových zkoušek. V poslední části je provedena simulace operace lisování svorky v různých směrech, dále vytvoření hyperelastického materiálového modelu elastomeru silentbloku, přes který je svorka zatěžovaná a provedena simulace nalisování silentbloku do svorky a její následné zatížení. Nakonec je proveden výpočet životnosti pomocí znalosti plastického přetvoření z lisování a napětí z jednoho zátěžného cyklu.

Klíčová Slova

Anisotropie, Plech, Tváření, Plasticita, Cyklická únava, Metoda konečných prvků

Declaration

I hereby declare that this thesis is my own work and is written only using referenced literature listed at the end of the thesis.

In Prague, 14.8.2022

_____

Author's signature

Acknowledgement

I would like to thank my supervisor, doc. Ing. Miroslav Španiel, CSc., for friendly approach, time and professional guidance in the process of writing this thesis. I would also like to thank my consultant Ing. Jaromír Kašpar, for friendly approach, patience and teaching me all the skills necessary to complete this task. Finally I would like to thank my family, friends and everyone else for all the support given to me during my studies.

Contents

List of Figures

List of Tables

Nomenclature

List of Abbreviations

DIC	Digital Image Correlation
FEA	Finite Element Method
S-N curve	Plot of applied stress against number of cycles to failure

List of Symbols

$\boldsymbol{C}$	Stiffness tensor of material properties
C_{pq}	Mooney-Rivlin material constant for distortional response
d	Incompressibility parameter
D_m	Mooney-Rivlin material constant for volumetric response
E	Young's modulus
E_p	Plastic modulus
E_t	Tangent modulus
$F(\sigma_{ij}), f(\sigma_{ij})$	Yield function
F, G, H, L, M, N	Hill's material parameters
$g(\sigma_{ij})$	Plastic potential function
I_j	Tensor invariant
J_i	Deviatoric stress tensor invariant
K	Material constant
K_i	Hardening parameter
n	Hardening exponent
r	r-value or Lankford parameter

r_n	Normal anisotropy
Δr	Planar anisotropy
R_{ij}	Yield stress ratio
s_{ij}	Deviatoric stress tensor
U_v	Volumetric (hydrostatic) strain energy density
U_d	Distortional strain energy density
α_{ij}	Tensorial hardening parameter or back stress
ϵ^p	Plastic strain
ϵ^e	Elastic strain
ϵ_{true}	True strain
ϵ_{eng}	Engineering strain
ϵ_{ij}	Strain tensor
$d\epsilon_{ij}$	Strain increment
$d\epsilon_{ij}^e$	Elastic strain increment
$d\epsilon_{ij}^p$	Plastic strain increment
λ, μ, G	Lamé parameters
$d\lambda$	Positive scalar factor of proportionality
μ	Friction coefficient
ν	Poisson's ratio
ρ	Density
σ_{ij}	Stress tensor
σ_H	Hydrostatic stress
σ_y	Tensile yield stress
σ_{true}	True stress
σ_{eng}	Engineering stress
$d\sigma$	Stress increment
τ_y	Shear yield stress
τ_{max}	Maximum shear stress
ψ, U	Strain energy density function

Chapter 1

Introduction

1.1 Motivation

Modern continuous rolling mills produce large quantities of thin sheet metal at low cost. A substantial fraction of all metals are produced as thin hot-rolled strip or cold rolled sheet; those are then formed in secondary processes into automobiles, domestic appliances, building products, aircraft, food and drink cans and a host of other familiar products. Sheet metals have the advantage of having a high elastic modulus and high yield strength, so the resulting parts can be stiff and have good strength-to-weight ratio.[1]

Due to their crystallographic structure and the charasteristics of the rolling processes, sheet metals generally exhibit a significant anisotropy of mechanical properties.

One of the most widely used techniques to manufacture components from sheet metal is forming, which is a process in which a piece of sheet metal is formed by stretching between a punch and a die. However various defects can occur; those include wrinkling, thinning, cracking, etc. It is also crucial to account for springback, since new materials such as high strength steel, aluminum and magnesium are particularly prone to it. In order to increase industrial performance, the concept of *virtual manufacturing* has been developed and has been one of the most efficient ways of reducing the manufacturing times and improving the quality of the products. Most notably, numerical simulation of forming processes has a big contribution to the reduction of the lead time and overall quality of the resultant components.

The Finite Element Analysis (FEA) is currently the most commonly used numerical method for simulating sheet metal forming processes. The accuracy of the numerical results varies depending on the *constitutive models* used. Consequently, in order to get realistic results, sufficient material models have to be built. [2]

1.2   Thesis Objectives

The main purpose of this work is to evaluate the influence anisotropy has on plastic straining and hardening resulting from forming processes. These are then used for a fatigue life estimation. The objectives of this thesis are listed below:

- create a suitalbe material model from available measurement data,

- confirm the validity of the material model by performing a FEA simulation of an uniaxial tensile test and compare results with the measured data,

- perform a FEA simulation of the forming process assuming both isotropic and anisotropic behaviour,

- evaluate loads exerted on the clamp in the fatigue life test through a pressed-in rubber bearing,

- perform a fatigue life calculation using FEMFAT software that accounts for material nonlinearities.

1.3   Structure of Thesis

In **Chapter 2** we introduce the basic overview of sheet metal anisotropy. Yield criteria for both isotropic and subsequently anisotropic materials are described in **Chapter 3**. **Chapter 4** is then focused on introducing the material model used, its properties and verification of proposed parameters. This material model is then used in **Chapter 5**, which concerns with the FEA simulation of the forming process, as well as a simulation of pressing in the rubber bearing. **Chapter 6** finally shows the simulation and results of fatigue life evaluation.

Chapter 2

Sheet Metal Anisotropy

2.1   Linear Elasticity and Hooke's Law

In the Theory of linear elasticity, a relationship between stress and strain is described by **Hooke's Law**. For one-dimensional case, consider a stress-strain curve $\sigma = f(\epsilon)$ of a linear elastic material subjected to uniaxial loading. For a given value of the strain, the *strain energy density* function $\psi = \psi(\epsilon)$ is defined as the area under the curve. In our case that is

$$\psi(\epsilon) = \frac{1}{2}E\epsilon^2 \tag{2.1}$$

We can then define the stress as

$$\sigma = \frac{\partial \psi}{\partial \epsilon} = E\epsilon \tag{2.2}$$

It shows that in an elastic material, strain is directly proportional to stress through the elasticity modulus. This proportionality is generalised for the multidimensional case in the **Generalized Hooke's Law**

$$\boldsymbol{\sigma} = \boldsymbol{C} : \boldsymbol{\epsilon} \tag{2.3}$$

where $\boldsymbol{C}$ is a 4th-order *stiffness* tensor of material properties. The strain energy density function for a general case becomes

$$\psi(\epsilon) = \frac{1}{2}C_{ijkl}\epsilon_{ij}\epsilon_{kl}. \tag{2.4}$$

This tensor has $3^4 = 81$ components and has following *minor* symmetries that result from the symmetry of the stress and strain tensors

$$\sigma_{ij} = \sigma_{ji} \implies C_{jikl} = C_{ijkl}. \tag{2.5}$$

This reduces the number of components from 81 to 54, and in a similar fashion we can use the symmetry of the strain tensor

$$\epsilon_{ij} = \epsilon_{ji} \implies C_{ijlk} = C_{ijkl} \tag{2.6}$$

and the number of components is further reduced to 36. Equation 2.2 for a general case becomes

$$\sigma_{ij} = \frac{\partial \psi}{\partial \epsilon_{ij}} = C_{ijkl}\epsilon_{kl}. \tag{2.7}$$

Differentiating this equation gives

$$\frac{\partial \psi^2}{\partial \epsilon_{mn}\partial \epsilon_{ij}} = \frac{\partial}{\partial \epsilon_{mn}}(C_{ijkl}\epsilon_{kl}) \tag{2.8}$$

$$\frac{\partial \psi^2}{\partial \epsilon_{mn}\partial \epsilon_{ij}} = C_{ijkl}\delta_{km}\delta_{ln} \tag{2.9}$$

$$C_{ijmn} = \frac{\partial \psi^2}{\partial \epsilon_{mn}\partial \epsilon_{ij}}. \tag{2.10}$$

If ψ is a sufficiently smooth function, we can assume equivalence of the mixed partials and we get *major* symmetry of the stiffness tensor

$$C_{ijkl} = \frac{\partial \psi^2}{\partial \epsilon_{ij}\partial \epsilon_{kl}} = \frac{\partial \psi^2}{\partial \epsilon_{kl}\partial \epsilon_{ij}} = C_{klij}. \tag{2.11}$$

Now the number of components drops to 21. The most general anisotropic linear elastic material - a material which doesn't exhibit any symmetry in material properties - then has 21 material constants [3]. A symmetric tensor can be represented by reducing its order (the so-called Voigt notation), so the stress-strain relation can be written as

$$\begin{bmatrix} \sigma_1 \\ \sigma_2 \\ \sigma_2 \\ \sigma_4 \\ \sigma_5 \\ \sigma_6 \end{bmatrix} = \begin{bmatrix} C_{11} & C_{12} & C_{13} & C_{16} & C_{15} & C_{16} \\ & C_{22} & C_{23} & C_{24} & C_{25} & C_{26} \\ & & C_{33} & C_{34} & C_{35} & C_{36} \\ & sym & & C_{44} & C_{45} & C_{46} \\ & & & & C_{55} & C_{56} \\ & & & & & C_{66} \end{bmatrix} \begin{bmatrix} \epsilon_1 \\ \epsilon_2 \\ \epsilon_3 \\ \epsilon_4 \\ \epsilon_5 \\ \epsilon_6 \end{bmatrix}. \tag{2.12}$$

2.2 Isotropic Elasticity

An *isotropic* material must have the same elastic properties in all directions. All components of $\mathbf{C}$ then must be independent of the orientation of the chosen coordinate system, therefore being *mathematically isotropic* tensor. A general form of this tensor is

$$C_{ijkl} = \lambda \delta_{ij}\delta_{kl} + \mu(\delta_{ik}\delta_{jl} + \delta_{il}\delta_{jk}), \qquad i,j,k,l \in 1,2,3 \tag{2.13}$$

where λ and μ are two independent material constants called *Lamé parameters*. Substituting into equation 2.7 we get

$$\sigma_{ij} = (\lambda \delta_{ij}\delta_{kl} + \mu(\delta_{ik}\delta_{jl} + \delta_{il}\delta_{jk}))\epsilon_{kl} \tag{2.14}$$

The resulting constitutive equation yields the **Generalized Hooke's Law for isotropic materials**

$$\sigma_{ij} = \lambda \delta_{ij} \epsilon_{kk} + 2\mu \epsilon_{ij} \tag{2.15}$$

where the Lamé parameters in terms of *Young's modulus E* and *Poisson's ratio ν* are

$$\lambda = \frac{\nu E}{(1+\nu)(1-2\nu)} \tag{2.16}$$

$$\mu = G = \frac{E}{2(1+\nu)} \tag{2.17}$$

2.3   Anisotropic Elasticity

An *anisotropic* material has directionally dependant material properties (mechanical or otherwise). The different types of material anisotropy are determined by the existence of symmetries in the internal structure of said material. The more symmetries occur, the simpler the structure of the stiffness tensor becomes. Each type of symmetry results in an invariance of the stiffness tensor to a specific *symmetry transformation* (rotations about specific axes and reflections with respect to specific planes).

The various classes of material symmetry include a *triclinic material*, which has no symmetry planes so therefore is fully anisotropic and has 21 material parameters, *monoclinic material* which has one symmetry plane and therefore has 13 material parameters and so on [3]. For our case, the important anisotropy class would be **ortothropic materials**. That is the behaviour that sheet metals exhibit and it has the following properties:

- three mutually orthogonal planes of reflection symmetry,

- 9 independent material parameters.

Based on those symmetries we get

$$\begin{bmatrix} \sigma_1 \\ \sigma_2 \\ \sigma_2 \\ \sigma_4 \\ \sigma_5 \\ \sigma_6 \end{bmatrix} = \begin{bmatrix} C_{11} & C_{12} & C_{13} & 0 & 0 & 0 \\ C_{21} & C_{22} & C_{23} & 0 & 0 & 0 \\ C_{31} & C_{32} & C_{33} & 0 & 0 & 0 \\ 0 & 0 & 0 & C_{44} & 0 & 0 \\ 0 & 0 & 0 & 0 & C_{55} & 0 \\ 0 & 0 & 0 & 0 & 0 & C_{66} \end{bmatrix} \begin{bmatrix} \epsilon_1 \\ \epsilon_2 \\ \epsilon_3 \\ \epsilon_4 \\ \epsilon_5 \\ \epsilon_6 \end{bmatrix} \tag{2.18}$$

2.4   Sheet Metal Anisotropy

As it was said before, due to their crystallographic structure and the characteristics of the rolling process, sheet metals generally tend to exhibit a significant anisotrpic mechanical behaviour. This particular behaviour, as mentioned previously, is called *orthotropic*. For rolled sheet metals, the orientation of the axes

of orthotropy is as follows: rolling direction (RD), transversal direction (TD) and normal direction (ND). Visualisation of these axes can be seen in Fig. 2.1.
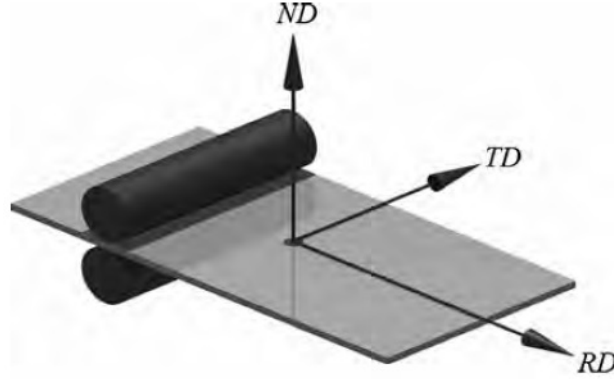
Figure 2.1: Orthotropy axes of rolled sheet metals.[2]

The difference in directional behaviour is often described by a measure called *Lankford parameters*, also often referred to as the *r-values*. These coefficients are determined experimentally by performing an uniaxial tensile test. These anisotropy coefficients are defined as

$$r = \frac{\epsilon_{22}}{\epsilon_{33}}, \tag{2.19}$$

where ϵ_{22} and ϵ_{33} are the strains in the transversal and normal directions ,respectively. Note that for isotropic materials, this coefficient is $r = 1$ - transversal and normal strains are equal. If the coefficient is $r > 1$, the strain in transversal direction will be dominant, and vice versa. Using the notation from Fig. 2.2, relation 2.19 can be written as

$$r = \frac{\ln \dfrac{w}{w_0}}{\ln \dfrac{l}{l_0}}. \tag{2.20}$$

Because the thickness of the specimen is in most cases at least one order lower than the width, the relative error in measurement of the normal strain is quite significant. Therefore it is often better to use the other two dimensions of the specimen; its length and width.[2] Assuming the condition of volume consistency

$$\epsilon_{11} + \epsilon_{22} + \epsilon_{33} = 0 \tag{2.21}$$

or

$$wtl = w_0 t_0 l_0 \tag{2.22}$$

and plugging in 2.19 we get

$$r = -\frac{\epsilon_{22}}{\epsilon_{11} + \epsilon_{22}}. \tag{2.23}$$
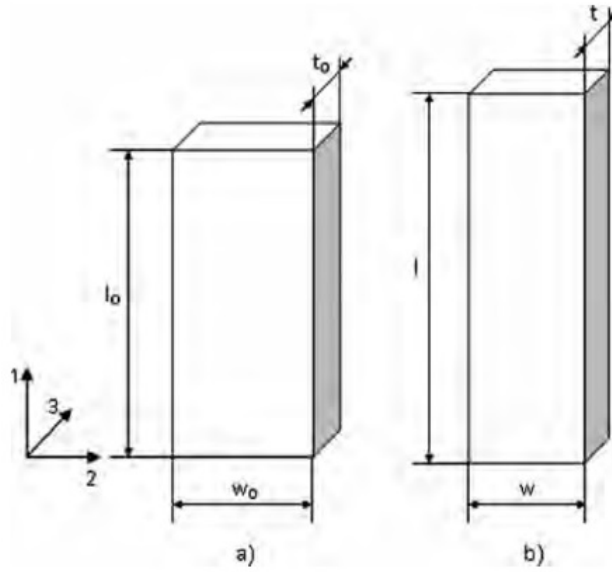
Figure 2.2: Notation for specimen deformations: (a) before deformation (b) after deformation.[2]

Once again, using the notation from Fig. 2.2, relation 2.21 becomes

$$r = -\frac{\ln\dfrac{w}{w_0}}{\ln\dfrac{l}{l_0} + \ln\dfrac{w}{w_0}}. \tag{2.24}$$

Using the properties of logarithms, we can rearrange the relation

$$r = \frac{\ln\dfrac{w}{w_0}}{\ln\dfrac{l_0 w_0}{lw}}. \tag{2.25}$$

Since the transversal strain is often measured continuously during the uniaxial tensile test, the Lankford parameters can be calculated continuously also. However, some variation in those parameters can be seen for different values of strain. Therefore, measurements are usually taken at a particular value of strain, e.g. at $e_{eng} = 15\%$ [1].

Experiments show that Lankford parameters depend on the in-plane direction. If the tensile specimen is cut having its longitudal axis inclined with the angle θ to the rolling direction, the coefficient r_θ is obtained (see Fig. 2.3), where the subscript specifies the angle between the angle the axis of the specimen and the rolling direction [2].

The most commonly used values are r_0, r_{45} and r_{90}, e.g. the Lankford parameters in the rolling, diagonal and transversal directions, respectively. In the general case, sheet metal display *planar anisotropy*, i.e. $r_0 \neq r_{45} \neq r_{90}$ and its
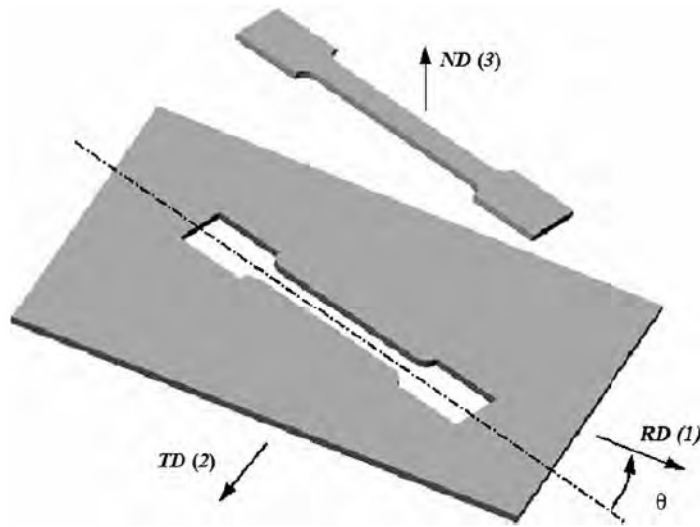
Figure 2.3: Tensile specimen prelevated at the angle θ (with respect to rolling direction).[2]

most common description is:

$$\Delta r = \frac{r_0 + r_{90} - 2r_{45}}{2} \qquad (2.26)$$

which may be positive or negative, but in steel it generally is positive. If the measured Lankford parameter differs from one, this shows a difference between average in-plane and through-thickness properties which is usually characterized by the *normal plastic anisotropy ratio*, defined as:

$$r_n = \frac{r_0 + 2r_{45} + r_{90}}{4}. \qquad (2.27)$$

The term 'normal' here is used in the sense of properties 'perpendicular' to the plane of the sheet.[1]

Chapter 3

Yield criteria

It is generally supposed that if an element of the ideal solid is plastically deformed, and then unloaded, it will recover elastically and in such a way that the change of strain depends linearly on the change of stress. During unloading, elastic recovery is limited by the plastic yielding of favourably oriented grains, but there is evidence to show that the elastic modulus, calculated from the initial slope of the unloading curve, remains invariant. The elastic constants of the ideal solid are therefore assumed to retain the same values provided they are defined with respect to the current shape of the element. Moreover, it is supposed that an element recovers its original shape when reloaded along the same path to the initial state of stress, and that there is no hysteresis loop. A law defining the limit of elasticity under any possible combination of stresses is known as a *yield criterion.*[4]

3.1   Yield Criteria for Isotropic Materials

In [2] Banabic says: In order to describe the plastic behaviour of a material in general stress state, three elements are needed:

- A yield criterion expressing a relationship between the stress components at the moment when plastic yielding occurs

- An associated flow rule expressing the relationship between the components of the strain-rate and stress

- A hardening rule describing the evolution of the initial yield stress during the forming process

For isotropic materials, we can always find the three principal stresses σ_1, σ_2 and σ_3 for a given stress tensor $\boldsymbol{\sigma}$. Since the material is considered isotropic, plastic yielding can then depend only on the magnitudes of these principal stresses, and not on their direction. Any yield function f can be expressed in the form

$$f(\boldsymbol{\sigma}) = f(\sigma_1, \sigma_2, \sigma_3) = 0. \tag{3.1}$$

Since the first three invariants of the stress tensor $\boldsymbol{\sigma}$ can be expressed in terms of the principal stresses, the yield criterion 3.1 can also be written as

$$f(\boldsymbol{\sigma}) = f(I_1, I_2, I_3) = 0. \tag{3.2}$$

The three fundamental invariants for any tensor $\boldsymbol{\sigma}$ are

$$I_1 = \text{tr}(\boldsymbol{\sigma}) = \sigma_{kk}, \tag{3.3}$$

$$I_2 = \frac{1}{2}((\text{tr}(\boldsymbol{\sigma}))^2 - \text{tr}(\boldsymbol{\sigma^2})) = \frac{1}{2}(\sigma_{ii}\sigma_{jj} - \sigma_{ij}\sigma_{ij}), \tag{3.4}$$

$$I_3 = \det(\boldsymbol{\sigma}) \tag{3.5}$$

and written in terms of principal stresses, these invariants become

$$I_1 = \sigma_1 + \sigma_2 + \sigma_3, \tag{3.6}$$

$$I_2 = \sigma_1\sigma_2 + \sigma_2\sigma_3 + \sigma_3\sigma_1, \tag{3.7}$$

$$I_3 = \sigma_1\sigma_2\sigma_3. \tag{3.8}$$

Here the invariants are the coefficients of the characteristic equation

$$-\lambda^3 + I_1\lambda^2 - I_2\lambda + I_3 = 0 \tag{3.9}$$

and the principal stresses σ_1, σ_2 and σ_3 are the roots [4][5].

We can immediately simplify Eq. 3.2 based on the fact that we can decompose a general triaxial stress state into stresses that cause a change in volume - so called *hydrostatic stresses* $\sigma_H \delta_{ij}$ - and stresses that cause a distortion of shape - so called *deviatoric stresses* s_{ij} as

$$\sigma_{ij} = \sigma_H \delta_{ij} + s_{ij}. \tag{3.10}$$

For the hydrostatic component σ_H, the principal stresses are always equal and there are no shear stresses. For the triaxial stress state we can simply obtain the hydrostatic component as an average of the three principal stresses

$$\sigma_H = \frac{1}{3}\sigma_{kk}. \tag{3.11}$$

Since plasticity is only a change in shape and not in volume, we know that only the deviatoric stress components are responsible for yielding. Finally we can say that Eq. 3.2 can be written in the form

$$f(\boldsymbol{\sigma}) = f(I_2, I_3) = 0. \tag{3.12}$$

We can also get the invariants of the deviatoric stress tensor s_{ij}

$$s_{ij} = \sigma_{ij} - \frac{1}{3}\sigma_{kk}\delta_{ij} \tag{3.13}$$

as

$$J_1 = s_{kk} = 0, \tag{3.14}$$

$$J_2 = \frac{1}{2}(s_{ii}s_{jj} - s_{ij}s_{ij}) = -\frac{1}{2}(s_{ij}s_{ij}), \tag{3.15}$$

$$J_3 = \det(\boldsymbol{s}) = \frac{1}{3}s_{ij}s_{jk}s_{ki}. \tag{3.16}$$

Then, the yield function can be written in terms of J_2 and J_3 as [5]

$$f(\boldsymbol{\sigma}) = f(J_2, J_3) = 0. \tag{3.17}$$

3.1.1   Tresca Yield Criterion

The simplest yield condition was proposed by Tresca in 1864 [6]. In his experiments, he observed that yielding occurred when the maximum shear stress reached a certain critical value. In other words, yielding occurs when the maximum shear stress is equal to the shear stress at yielding in an uniaxial tensile test. In general case the maximum shear stress τ_{max} can be conveniently obtained in terms of the maximum difference of the three principal stresses σ_1, σ_2 and σ_3 (see Fig. 3.1) as

$$\tau_{max} = \frac{1}{2}\max(|\sigma_1 - \sigma_2|, |\sigma_2 - \sigma_3|, |\sigma_3 - \sigma_1|). \tag{3.18}$$
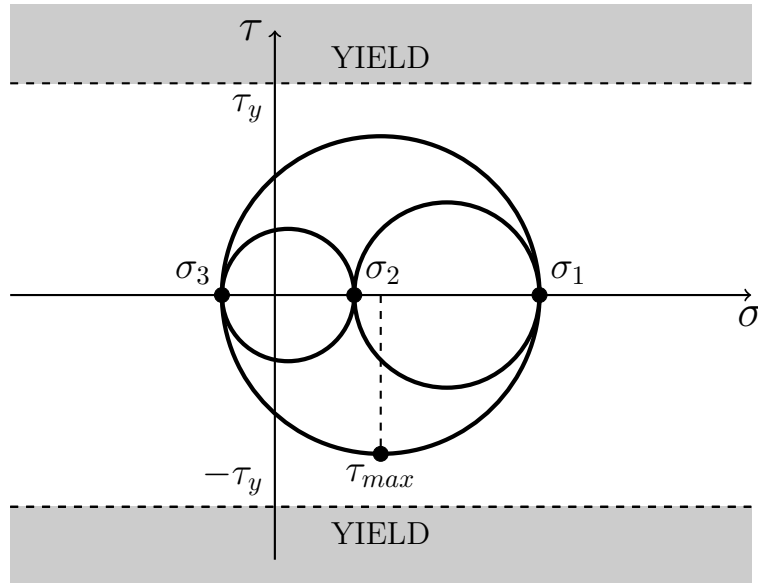

Figure 3.1: Mohr circles for a general triaxial stress.

When the maximum shear stress τ_{max} reaches the shear yield stress τ_0, the Tresca yield condition is satisfied. Therefore, the Tresca yield condition is written as

$$\max(|\sigma_1 - \sigma_2|, |\sigma_2 - \sigma_3|, |\sigma_3 - \sigma_1|) = 2\tau_y \tag{3.19}$$

Uniaxial tensile tests are usually performed in order to get the stress-strain curve of the material so the relation between the tensile yield stress σ_y and shear yield stress τ_y is needed (see Fig. 3.2):

$$\frac{\sigma_1 - \sigma_3}{2} = \tau_y = \frac{\sigma_y}{2} \implies \sigma_y = 2\tau_y. \tag{3.20}$$
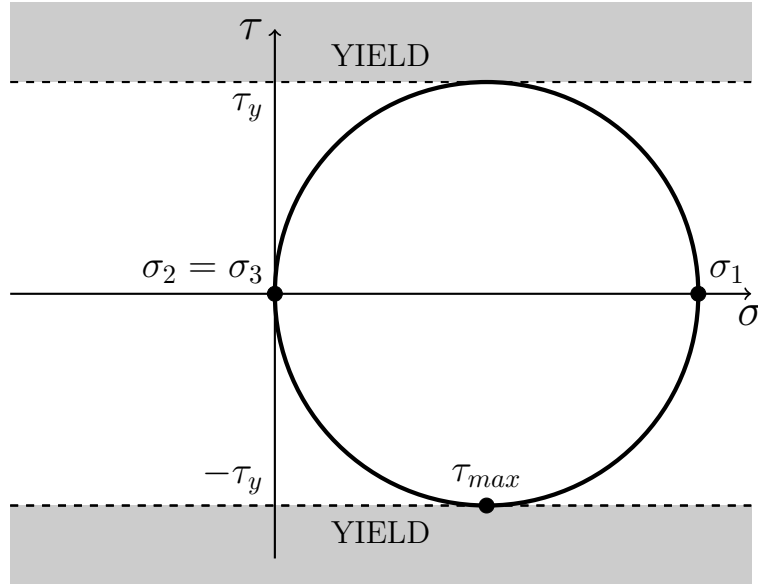
Figure 3.2: Mohr circle for the uniaxial tensile test.

3.1.2   von Mises Yield Criterion

This criterion, sometimes called Maxwell-Huber-Hencky-von Mises theory, also arises from the observation that plastic yielding is only caused by deviatoric stresses. It states that yielding will occur for a general 3D stress state when the combination of stresses reaches the maximum distortional strain energy density. The strain energy density U (strain energy per unit volume) can be decomposed as

$$U = U_v + U_d \tag{3.21}$$

where U_v is the *volumetric* (hydrostatic) strain energy density and U_d is the *distortional* strain energy density. Since only the distortion component causes yielding, we rearrange Eq. 3.21

$$U_d = U - U_v. \tag{3.22}$$

The total strain energy density takes the form

$$U = \frac{1}{2E}\left[\sigma_1^2 + \sigma_2^2 + \sigma_3^2 - 2\mu(\sigma_1\sigma_2 + \sigma_2\sigma_3 + \sigma_3\sigma_1)\right]. \tag{3.23}$$

This for the volumetric component becomes

$$U_v = \frac{3\sigma_H^2}{2E}(1 - 2\nu) \tag{3.24}$$

and if we plug in the expression for hydrostatic pressure, we get

$$U_v = \frac{1 - 2\nu}{6E}\left[\sigma_1^2 + \sigma_2^2 + \sigma_3^2 + \sigma_1\sigma_2 + \sigma_2\sigma_3 + \sigma_3\sigma_1\right]. \tag{3.25}$$

Now, substituting back into 3.22 finally gives the distortional strain energy density

$$U_d = \frac{1 + \nu}{6E}\left[(\sigma_1 - \sigma_2)^2 + (\sigma_2 - \sigma_3)^2 + (\sigma_3 - \sigma_1)^2\right]. \tag{3.26}$$

Once again, yielding during uniaxial tensile test occurs when $\sigma_2 = \sigma_3 = 0$ and $\sigma_1 = \sigma_y$. Plugging into Eq. 3.26, U_d takes the form

$$U_d = \frac{1 + \nu}{3E}\sigma_y^2 \tag{3.27}$$

and now comparing the right hand sides of the two previous equations, we can write the von Mises yield criterion in terms of principal stresses as

$$f(\sigma) = \frac{1}{2}\left[(\sigma_1 - \sigma_2)^2 + (\sigma_2 - \sigma_3)^2 + (\sigma_3 - \sigma_1)^2\right] - \sigma_y^2 = 0 \tag{3.28}$$

or for a general stress state as [2][3][7]

$$f(\sigma) = \frac{1}{2}\left[(\sigma_{11} - \sigma_{22})^2 + (\sigma_{22} - \sigma_{33})^2 + (\sigma_{33} - \sigma_{11})^2 + 6(\sigma_{23}^2 + \sigma_{31}^2 + \sigma_{12}^2)\right] = 0 \tag{3.29}$$

3.1.3   Plane Stress Yield Criteria for Isotropic Materials

Due to the geometry of sheet metals, i.e. the thickness being much smaller than the width and length, plane stress is often assumed. This is shown in Fig. 3.3. Under plane stress conditions, we only consider the in-plane stresses σ_{11}, σ_{22} and the in-plane shear stress σ_{12}. The out-of-plane normal stress σ_{33} and the out-of-plane shear stresses σ_{13} and σ_{23} are assumed to be zero. The von Mises yield condition 3.28 reduces to

$$f(\sigma) = \sigma_{11}^2 + \sigma_{22}^2 - \sigma_{11}\sigma_{22} + 3\sigma_{12}^2 = \sigma_y^2. \tag{3.30}$$

We can write Eq. 3.30 in terms of the in-plane principal stresses σ_1 and σ_2 as

$$f(\sigma) = \sigma_1^2 + \sigma_2^2 - \sigma_1\sigma_2 = \sigma_y^2 \tag{3.31}$$

Similarly, the Tresca yield criterion 3.19 in terms of the in-plane principal stresses

$$\max(|\sigma_1 - \sigma_2|, |\sigma_1|, |\sigma_2|) = \sigma_y \tag{3.32}$$
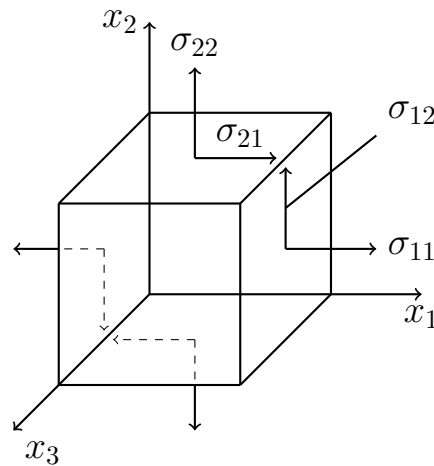
Figure 3.3: Element of sheet metal under plane stress conditions.

We can plot both yield criteria in a 2D principal stress space. It can be seen that the von Mises condition is an ellipse resulting from the intersection of a cylindrical yield surface with the plane for $\sigma_3 = 0$. For the Tresca criterion, if we consider all possible combinations of the in-plane stresses σ_1 and σ_2, we get a set of equations

$$|\sigma_1 - \sigma_2| = \sigma_y \tag{3.33}$$

$$|\sigma_1| = \sigma_y \tag{3.34}$$

$$|\sigma_2| = \sigma_y. \tag{3.35}$$

Plotted in the $\sigma_1 - \sigma_2$ plane, we get a hexagon as seen in Fig 3.4. The von Mises
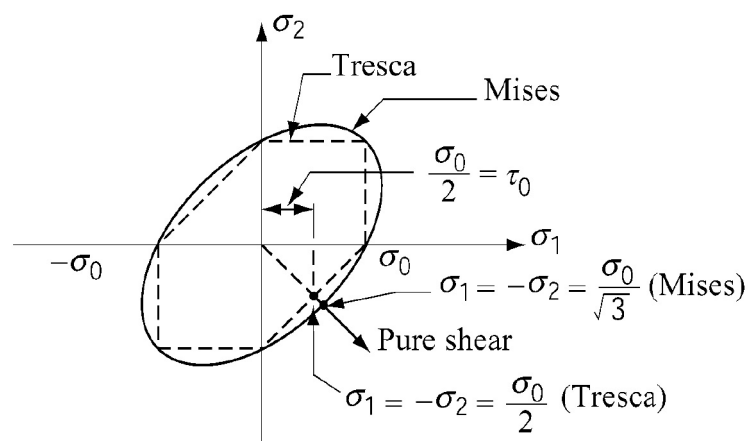

Figure 3.4: The von Mises and Tresca yield conditions.[5]

criterion is used more often as it better agrees with experimental data. However,

the Tresca criterion can still find its uses due to it being easier to implement and being more conservative [5].

For a general stress state $\sigma_3 \neq 0$, we can once again use the knowledge that the Tresca and von Mises yield surfaces aren't affected by hydrostatic stress components. To obtain the yield surfaces in 3D stress space, we only need to extend plane stress surfaces along the hydrostatic axis as seen in Fig. 3.5.
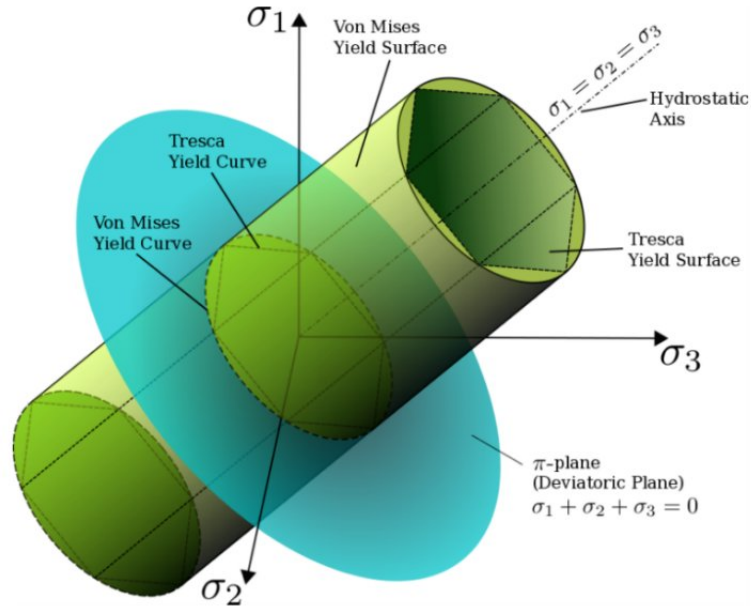

Figure 3.5: The von Mises and Tresca yield surfaces in 3D [23]

3.1.4   Modeling of Uniaxial Plasticity

Different Models for Uniaxial Stress-Strain Curves

The stress-strain curves are quite different for different metals. Since it is often difficult to determine the yield point due to the behaviour of certain materials when yielding occurs, the 0.2% strain offset is usually used to determine the yield stress σ_y as seen in Fig. 3.6. It can also be seen that as the strain continues to increase, the stress increases non-linearly. When the strain decreases, so does the stress and the stress-strain curve usually follows the curve with the slope of the Young's elastic modulus E. This means when the stress drops to zero, the strain only reduces by the elastic amount ϵ^e and there is some non-recoverable plastic strain ϵ^p. Within the context of small strain approach, the total strain ϵ can be decomposed as

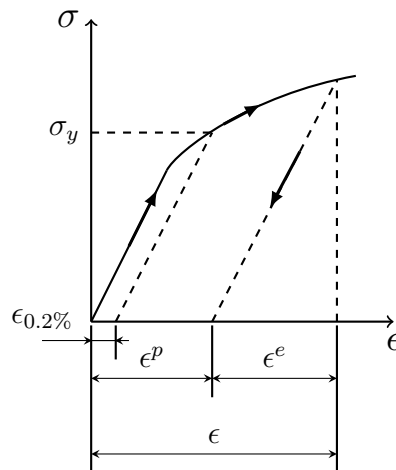$$\epsilon = \epsilon^e + \epsilon^p \tag{3.36}$$

Figure 3.6: Elastic, plastic, total and the 0.2% offset strains.

Generally, different simplifications for tensile stress-strain curves are used. In some instances, it is permissible and convenient to neglect the effect of work hardening, two of which will be shown. The simplest one is a rigid perfectly plastic idealization as seen in Fig. 3.7(a). It can be seen that there is assumed to be no elastic strain and no strain hardening. The total strain ϵ is then equal to the plastic strain ϵ^p

$$\epsilon = \epsilon^p. \tag{3.37}$$

Another simple model, called elastic perfectly plastic, can be seen in Fig. 3.7(b). This model is usually used when we need to examine the elastic-plastic response of a region that exhibits both elastic and plastic deformation. From Hooke's law we know that the elastic deformation is

$$\epsilon^e = \frac{\sigma_y}{E} \tag{3.38}$$

and the total strain is therefore

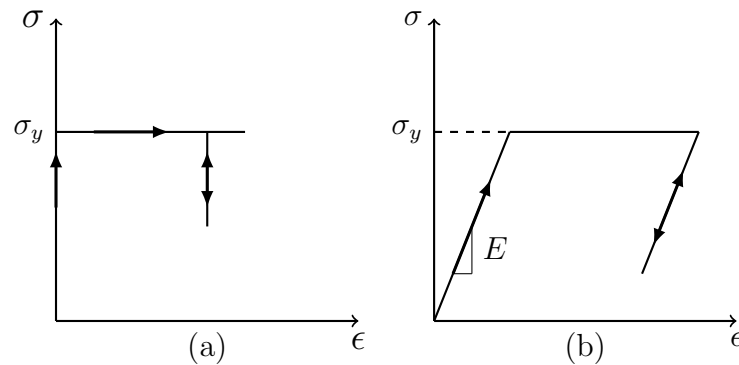$$\epsilon = \frac{\sigma_y}{E} + \epsilon^p \tag{3.39}$$

Figure 3.7: (a) Rigid perfectly plastic and (b) elastic perfectly plastic models.

Figure 3.8 depicts two models that assume linear plastic straining, specifically the rigid linear strain hardening model (Fig. 3.8(a)) and the elastic linear strain hardening model (Fig. 3.8(b)). For the first case, the elastic strain ϵ^e is once again considered zero and the plastic strain ϵ^p can be written as

$$\epsilon = \epsilon^p = \frac{\sigma - \sigma_y}{E_t} \tag{3.40}$$

where E_t is the tangent modulus and is defined as the slope of the plastic stress-strain curve. For the second model, again similarly to the perfectly plastic idealizations, we don't neglect the elastic strain ϵ^e and the total strain ϵ then becomes

$$\epsilon = \frac{\sigma_y}{E} + \frac{\sigma - \sigma_y}{E_t}. \tag{3.41}$$

Note that linear strain hardening is usually used to save computational time since the stiffness matrix of the elastic-plastic finite element formulation remains unchanged during iterations for plastic loading.
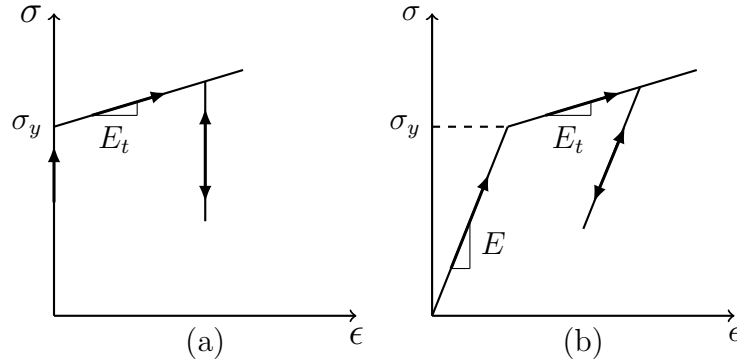

Figure 3.8: (a) Rigid perfectly plastic and (b) elastic perfectly plastic models.

However, we often need to describe the non-linear behaviour in the plastic region, which is where power-law strain hardening models come in. Fig. 3.9(a) shows the pure power-law strain hardening model and Fig. 3.9(b) shows the elastic power-law strain hardening model. Again, no elastic strain ϵ^e is assumed for the pure power-law and it can be written in the form

$$\epsilon = \epsilon^p = \left(\frac{\sigma}{K}\right)^{\frac{1}{n}} \tag{3.42}$$

or equivalently

$$\sigma = K\epsilon^n. \tag{3.43}$$

Here, n is the hardening exponent and K is a material constant. For the elastic power-law it can be seen that [5]

$$\sigma = E\epsilon \quad \text{for} \quad \sigma \leq \sigma_y \tag{3.44}$$

$$\sigma = K\epsilon^n \quad \text{for} \quad \sigma > \sigma_y \tag{3.45}$$
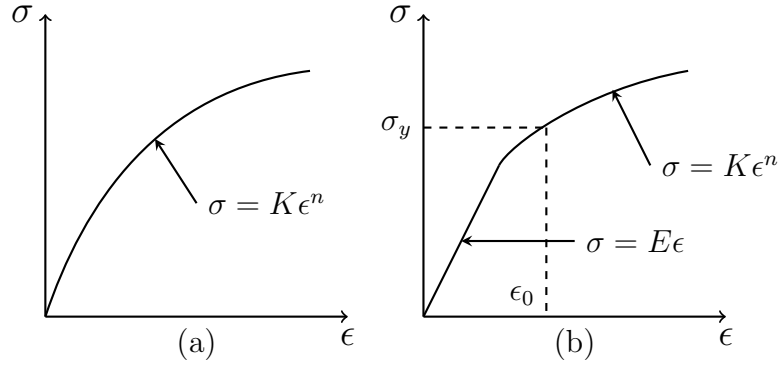
Figure 3.9: (a)Pure power-law and (b) elastic power-law models.

Tangent Modulus E_t and Plastic Modulus E_p

Because of the nonlinear nature of the elastic-plastic stress-strain response of a material, an incremental approach is generally used in solution of a deformation problem. The *strain increment $d\epsilon$* is assumed to consist of two parts: the *elastic strain increment $d\epsilon^e$* and the *plastic strain increment $d\epsilon^p$*, such that

$$d\epsilon = d\epsilon^e + d\epsilon^p \tag{3.46}$$

where in the case of uniaxial loading, E_t is the current slope of the $\sigma - \epsilon$ curve as seen in Fig. 3.10(a). The *stress increment $d\sigma$* is related to the strain increment $d\epsilon$ by

$$d\sigma = E_t d\epsilon \tag{3.47}$$

If we separate the plastic strain ϵ^p from the total strain ϵ , then the plastic strain increment $d\epsilon^p$ and the stress increment $d\sigma$ are related by

$$d\sigma = E_p d\epsilon^p \tag{3.48}$$

where E_p is the *plastic modulus*, which in the case of uniaxial loading is the slope of the $\sigma - \epsilon^p$ curve as seen in Fig. 3.10(b). Elastic strain increment $d\epsilon^e$ is given as usual

$$d\sigma = E d\epsilon^e \tag{3.49}$$

Plugging these three relations into equation 3.46 yields the relationship between the three moduli [8] E,E_t and E_p

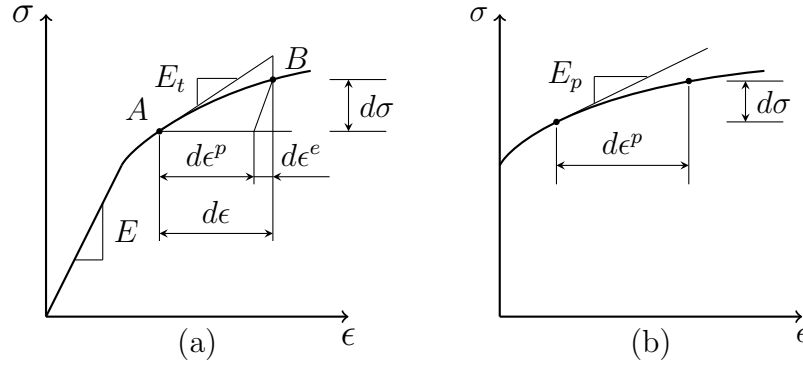$$\frac{1}{E_t} = \frac{1}{E} + \frac{1}{E_p}. \tag{3.50}$$

Figure 3.10: (a) Tangent modulus E_t and (b) plastic modulus E_p.

3.2   Hardening

Once the material passes the yield point, it begins to strain non-linearly as the stress needs to be continually increased in order to drive the plastic deformation. If the stress is then reduced, elastic unloading occurs. This process can cause the yield surface to change in size, shape or position with plastic deformation and can be described by

$$f(\sigma_{ij}, K_i) = 0 \qquad (3.51)$$

where K_i represents one or more *hardening parameters*. Equation 3.51 is called the *hardening rule* [9].

3.2.1   Hardening rules

Isotropic Hardening

The isotropic hardening rule assumes that the initial yield surface expands uniformly and no distortion or translation occurs with plastic flow. This can be seen in Fig. 3.11. We can express the equation for the subsequent yield surface in the form

$$F(\sigma_{ij}) = k^2(\epsilon^p). \qquad (3.52)$$

For example, we can use the von Mises initial yield function, we get

$$J_2 = \frac{1}{2} s_{ij} s_{ij} = k^2(\epsilon^p) \qquad (3.53)$$

and if we use the von Mises effective stress σ_e, equation 3.52 becomes [8]

$$f(\sigma_{ij}, k) = \frac{3}{2} s_{ij} s_{ij} - \sigma_e^2(\epsilon^p) = 0. \qquad (3.54)$$

This formulation of the isotropic hardening rule will later be used in our Finite Element Analysis.
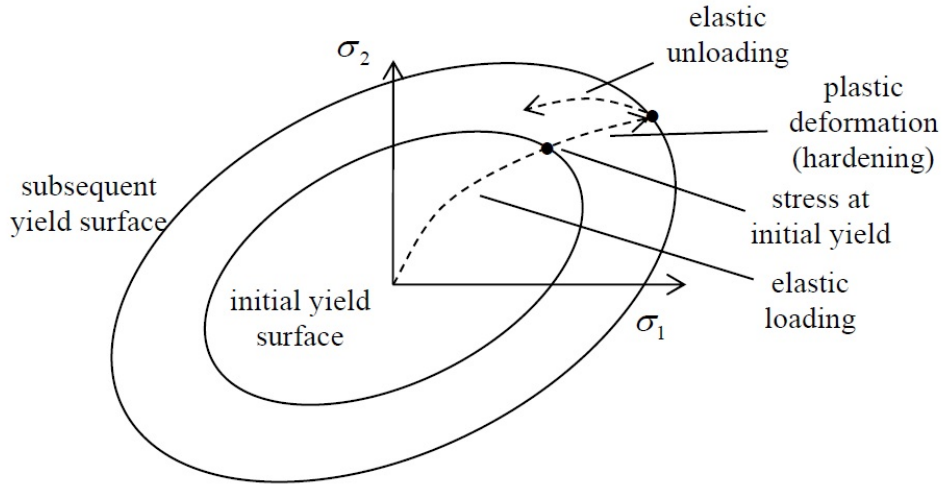
Figure 3.11: Isotropic hardening - evoluton of the yield surface.[9]

Kinematic Hardening

The kinematic hardening rule assumes that during plastic deformation, the yield surface translates in stress space without a change in size, shape and orientation of the initial yield surface (see Fig. 3.12). In order to determine the new position of the yield surface, we introduce a tensorial hardening parameter α_{ij}, called the *back stress*, which represents the shift of the origin of the yield surface. We can describe the subsequent yield surface by the equation [8]

$$f(\sigma_{ij}, \alpha_{ij}, K) = F(\sigma_{ij} - \alpha_{ij}) - K^2 = 0 \tag{3.55}$$

where K is a constant. If we once agian use the von Mises function, equation 3.55 becomes

$$f(\sigma_{ij}, \alpha_{ij}, K) = \frac{1}{2}(s_{ij} - \alpha_{ij})(s_{ij} - \alpha_{ij}) - K^2 = 0. \tag{3.56}$$

Note that as a rigid-body translation of the yield surface, the kinemactic hardening rule predicts an ideal Bauschinger effect.
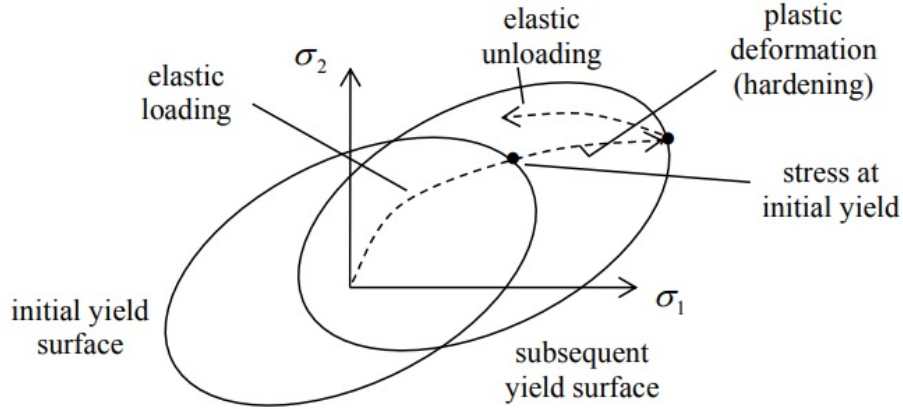
Figure 3.12: Kinematic hardening - evoluton of the yield surface.[9]

3.3   Flow Rule

3.3.1   Associative and Non-Associative Flow Rules

In elasticity theory, the elastic strain can be directly derived by differentiating the *elastic potential function* with respect to stresses σ_{ij}

$$\epsilon_{ij} = \frac{\partial U_e}{\partial \sigma_{ij}}. \tag{3.57}$$

In 1928 Von Mises proposed a similar concept [10]; he proposed that there existed a *plastic potential function* $g(\sigma_{ij})$, and that the plastic strain increment $d\epsilon_{ij}^p$ can be derived as

$$d\epsilon_{ij}^p = d\lambda \frac{\partial g}{\partial \sigma_{ij}} \tag{3.58}$$

where $d\lambda$ is a *positive scalar factor of proportionality*. This factor is only non-zero when plastic deformation occurs. Equation 3.58 is called a *flow rule* and the plasticity theory based on it is called the *plastic potential theory*. [11] If we take the equation $g(\sigma_{ij}) = const.$, we get a surface in stress space. Geometrically, equation 3.58 implies that the plastic flow vector $d\epsilon_{ij}^p$ is directed along the normal to this surface. We are particulary interested in a case where the plastic potential function $g(\sigma_{ij})$ is equal to a yield function $f(\sigma_{ij})$, so that

$$d\epsilon_{ij}^p = d\lambda \frac{\partial f}{\partial \sigma_{ij}}. \tag{3.59}$$

The plastic flow develops along the normal to the yield surface $\partial f / \partial \sigma_{ij}$ and the equation 3.59 is called an *associated flow rule*, since it is associated to a certain yield criterion. A general case as seen in equation 3.58 is called a *non-associated flow rule*.[8]

3.3.2   Von Mises Associated Flow Rule

Let us now consider the von Mises condition

$$f(\sigma_{ij}) = J_2^2 - k^2 = 0. \tag{3.60}$$

Plugging into the equation 3.59 we get

$$d\epsilon_{ij}^p = d\lambda \frac{\partial f}{\partial \sigma_{ij}} = d\lambda s_{ij}. \tag{3.61}$$

The factor of proportionality $d\lambda$ takes values

$$d\lambda \begin{cases} = 0 & \text{if } J_2 < k^2 \text{ or } J_2 = k^2, \text{ but } dJ_2 < 0 \\ > 0 & \text{if } J_2 = k^2 \text{ and } dJ_2 = 0. \end{cases}$$

If we write equation 3.60 in terms of the components, we obtain

$$\frac{d\epsilon_x^p}{s_x} = \frac{d\epsilon_y^p}{s_y} = \frac{d\epsilon_z^p}{s_z} = \frac{d\gamma_{yz}^p}{2\tau_{yz}} = \frac{d\gamma_{zx}^p}{2\tau_{zx}} = \frac{d\gamma_{xy}^p}{2\tau_{xy}} = d\lambda. \tag{3.62}$$

Relations 3.62 are know as the *Prandtl-Reuss* equations. They describe a general stress-strain relation for an elastic-perfectly plastic material. Note that these equations are an extension to the so called *Levy-Mises* equations

$$\frac{d\epsilon_x}{s_x} = \frac{d\epsilon_y}{s_y} = \frac{d\epsilon_z}{s_z} = \frac{d\gamma_{yz}}{2\tau_{yz}} = \frac{d\gamma_{zx}}{2\tau_{zx}} = \frac{d\gamma_{xy}}{2\tau_{xy}} = d\lambda \tag{3.63}$$

which neglect elastic strain and are used in problems where large plastic flow occurs [8].

3.4   Yield Criteria for Anisotropic Materials

Despite the fact that we can approximate a large range of materials as isotropic, strictly speaking, all materials behave anisotropic to some extent. Many anisotropic yield functions have been proposed over the years, some examples being Hill ([12], [13]), Hershey [14], Logan and Hosford [15] [16], Karafillis and Boyce [17], Barlat *et al.* [18][19][20] and others. However, the additional plastic anisotropy developed due to large plastic strains during forming is typically way too complex to be included in the practical application of sheet forming simulations [5]. In this thesis we will focus in one in particular and that being Hill's 1948 yield criterion.

3.4.1   Hill's 1948 Yield Criterion

This criterion has been proposed by Hill as a generalization of the von Mises yield criterion. Let's consider the same axes of orthotropy as in Chapter 2; rolling direction (RD), transversal direction (TD) and normal direction (ND) (see Fig. 3.13)
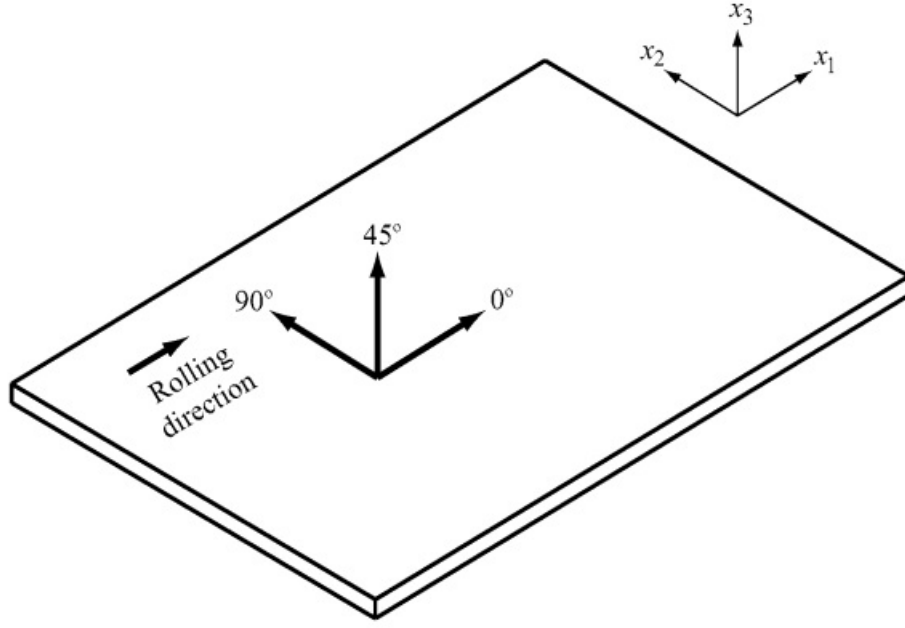
Figure 3.13: Axes direction.[5]

The yield function has the form

$$
\begin{aligned}
f(\sigma_{ij}) =& F(\sigma_{22} - \sigma_{33})^2 + G(\sigma_{33} - \sigma_{11})^2 + H(\sigma_{11} - \sigma_{22})^2 \\
& + 2L\sigma_{23}^2 + 2M\sigma_{31}^2 + 2N\sigma_{12}^2 - \bar{\sigma}^2 = 0
\end{aligned}
\tag{3.64}
$$

where $\bar{\sigma}$ is the refference yield stress and F, G, H, L, M, N are material parameters that can be determined experimentally; in principle by tensile and shear tests with respect to different orientations. In sheet metals, we usually have the anisotropic behaviour described using the r-values. Therefore, it is useful to express the material constants F, G, H, L, M, N in terms of r_0, r_{45} and r_{90}. In order to do that, let us take Hill's yield function 3.64 as our plastic potential, so that the associated flow rule gives

$$
d\epsilon_{11}^p = d\lambda \frac{\partial f}{\partial \sigma_{11}} = d\lambda \big[- 2G(\sigma_{33} - \sigma_{11}) + 2H(\sigma_{11} - \sigma_{22}) \big]
\tag{3.65}
$$

$$
d\epsilon_{22}^p = d\lambda \frac{\partial f}{\partial \sigma_{22}} = d\lambda \big[2F(\sigma_{22} - \sigma_{33}) - 2H(\sigma_{11} - \sigma_{22}) \big]
\tag{3.66}
$$

$$
d\epsilon_{33}^p = d\lambda \frac{\partial f}{\partial \sigma_{33}} = d\lambda \big[- 2F(\sigma_{22} - \sigma_{33}) + 2G(\sigma_{33} - \sigma_{11}) \big]
\tag{3.67}
$$

$$2d\epsilon_{23}^p = d\lambda \frac{\partial f}{\partial \sigma_{23}} = d\lambda \big[4L\sigma_{23} \big] \tag{3.68}$$

$$2d\epsilon_{31}^p = d\lambda \frac{\partial f}{\partial \sigma_{31}} = d\lambda \big[4M\sigma_{31} \big] \tag{3.69}$$

$$2d\epsilon_{12}^p = d\lambda \frac{\partial f}{\partial \sigma_{12}} = d\lambda \big[4N\sigma_{12} \big] \tag{3.70}$$

First let us consider uniaxial loading in rolling direction, so that $\sigma_{11} \neq 0$ and $\sigma_{22} = \sigma_{33} = \sigma_{23} = \sigma_{31} = \sigma_{12} = 0$. Based on the definition of r-values (see Eq. 2.19)

$$r_0 = \frac{d\epsilon_{22}^p}{d\epsilon_{33}^p} = \frac{H}{G}. \tag{3.71}$$

Similarly, considering uniaxial loading in transversal direction, so that $\sigma_{22} \neq 0$ and $\sigma_{11} = \sigma_{33} = \sigma_{23} = \sigma_{31} = \sigma_{12} = 0$ we get

$$r_{90} = \frac{d\epsilon_{11}^p}{d\epsilon_{33}^p} = \frac{H}{F}. \tag{3.72}$$

To get the r_{45} value, assume we rotate the orthotropic coordinate system 45° counterclockwise with respect to the normal axis. Let's denote the axes of this rotated system x_1', x_2', x_3'. Now, let's again assume uniaxial loading in the x_1' direction. The stress transformation gives the stress components with respect to the original orthotropic axes as $\sigma_{11} = \sigma_{22} = \sigma_{12} = \sigma/2$. Using the above derived relations, we get

$$d\epsilon_{11}^p = d\lambda G\sigma \tag{3.73}$$

$$d\epsilon_{22}^p = d\lambda F\sigma \tag{3.74}$$

$$d\epsilon_{12}^p = d\lambda N\sigma. \tag{3.75}$$

Based on the transformation, the transverse plastic strain rate $\epsilon_{22}^{p'}$ with respect to the rotated coordinate system x_1', x_2', x_3' is

$$d\epsilon_{22}'^p = d\lambda \frac{1}{2} \big[G\sigma + F\sigma - 2N\sigma \big]. \tag{3.76}$$

We know that $d\epsilon_{33}'^p = d\epsilon_{33}^p$ and we get

$$d\epsilon_{33}'^p = d\lambda \big[-F\sigma - G\sigma \big]. \tag{3.77}$$

r_{45} then can be written as

$$r_{45} = \frac{d\epsilon_{22}'^p}{d\epsilon_{33}'^p} = \frac{2N - (F+G)}{2(F+G)}. \tag{3.78}$$

Finally, plugging $\sigma_y^x = \bar{\sigma}$ in Eq. 3.64 yields

$$G + H = 1. \tag{3.79}$$

Solving for F, G, H and N gives [5]

$$F = \frac{r_0}{r_{90}(1 + r_0)} \tag{3.80}$$

$$G = \frac{1}{1 + r_0} \tag{3.81}$$

$$H = \frac{r_0}{1 + r_0} \tag{3.82}$$

$$N = \frac{(2r_{45} + 1)(r_0 + r_{90})}{2r_{90}(1 + r_0)}. \tag{3.83}$$

3.4.2   ANSYS Implementation

ANSYS FEA software uses Hill's 1948 criterion to account for anisotropic yield of the material. Using a multilinear isotropic hardening option, the yield function is given by

$$f\{\sigma\} = \sqrt{\{\sigma\}^T [M]\{\sigma\}} - \sigma_0(\bar{\epsilon}^p) \tag{3.84}$$

Here, σ_0 is the reference yield stress and $\bar{\epsilon}^p$ is the equivalent plastic strain. The matrix M has the form

$$[M] = \begin{bmatrix} G+H & -H & -H & 0 & 0 & 0 \\ -H & F+H & -F & 0 & 0 & 0 \\ -G & -F & F+G & 0 & 0 & 0 \\ 0 & 0 & 0 & 2N & 0 & 0 \\ 0 & 0 & 0 & 0 & 2L & 0 \\ 0 & 0 & 0 & 0 & 0 & 2M \end{bmatrix} \tag{3.85}$$

Since we are working with sheet metal anisotropy, we assume that $N = L = M$. The above material constants F, G, H and N can also be defined in terms of yield stress ratios as

$$F = \frac{1}{2}\left(\frac{1}{R_{yy}^2} + \frac{1}{R_{zz}^2} - \frac{1}{R_{xx}^2}\right) \tag{3.86}$$

$$G = \frac{1}{2}\left(\frac{1}{R_{zz}^2} + \frac{1}{R_{xx}^2} - \frac{1}{R_{yy}^2}\right) \tag{3.87}$$

$$H = \frac{1}{2}\left(\frac{1}{R_{xx}^2} + \frac{1}{R_{yy}^2} - \frac{1}{R_{zz}^2}\right) \tag{3.88}$$

$$N = \frac{3}{2}\left(\frac{1}{R_{xy}^2}\right) \tag{3.89}$$

where

$$R_{xx} = \frac{\sigma_{xx}^y}{\sigma_0} \tag{3.90}$$

$$R_{yy} = \frac{\sigma_{yy}^y}{\sigma_0} \tag{3.91}$$

$$R_{zz} = \frac{\sigma_{zz}^y}{\sigma_0} \tag{3.92}$$

$$R_{xy} = \sqrt{3}\frac{\sigma_{xy^y}}{\sigma_0} \tag{3.93}$$

These yield stress ratios are then used as the user input for Hill's criterion in ANSYS Workbench [21].

Chapter 4

Material Model

4.1 Measured Data

The material in question is a steel S420MC. 12 specimens were subjected to the uniaxial tensile test; 4 in the rolling direction (0°), 4 in the transversal direction (90°) and 4 at 45° angle from the rolling direction axis. Another 4 specimens were subjected to the compression test.

4.1.1 Uniaxial Testing

The uniaxial tensile tests were conducted at room temperature of 23°C with a constant speed of 4.8 mm/min on a servo-electric machine with a capacity of 100 kN (see Fig. 4.2). Optical measuring system that uses the digital image correlation (DIC) technique (see Fig. 4.1) was used to get a precise deformation measurements. The specimen geometry can be seen in Fig. 4.3 (thickness of the specimen is $T = 4$ mm).
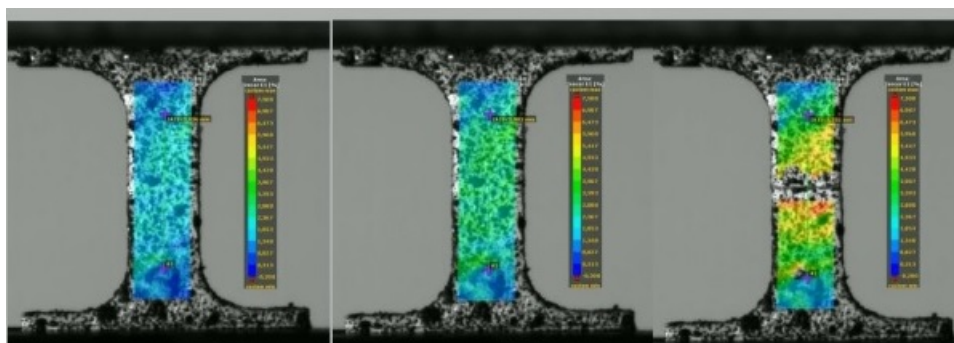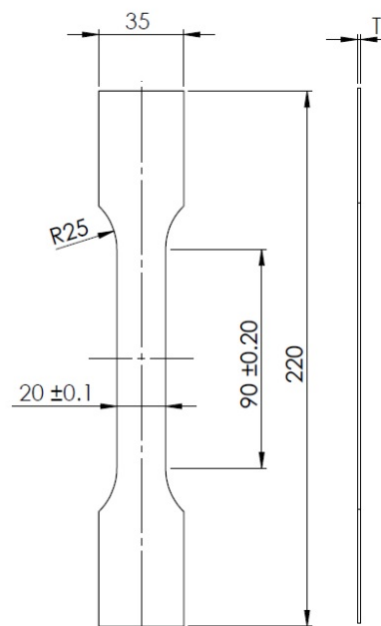

Figure 4.1: Example of DIC. [Comtes]

Figure 4.2: Tensile testing rig.[Comtes]

Figure 4.3: Geometry of the specimen. [Comtes]

Table 4.1: Measured data.

Specimen	a_u mm	b_u mm	$R_{p0.2}$ MPa	R_m MPa	r_{3-5}	r_{3-8}	r_{3-Ag}
S420MC_0_1	1.43	15.78	464.2	540.7	0.704149	0.702717	0.696871
S420MC_0_2	1.47	15.69	463.5	540.1	0.723209	0.727818	0.720976
S420MC_0_3	1.49	15.56	460.5	536.9	0.708237	0.724129	0.728306
S420MC_0_4	1.41	16.18	470.3	540.3	0.549035	0.551070	0.539978
Average			464.6	539.5			0.671533
S420MC_45_1	1.78	13.75	473.9	528.4	1.153161	1.158858	1.178842
S420MC_45_2	1.64	13.48	472.4	529.4	1.194890	1.184881	1.178398
S420MC_45_3	1.75	13.78	462.7	528.3	3.003120	2.955696	2.904226
S420MC_45_4	1.72	13.62	468.4	527.0	1.149190	1.154486	1.162716
Average			469.3	528.3			1.173319
S420MC_90_1	1.76	14.96	489.0	552.1	0.806419	0.793218	0.784508
S420MC_90_2	1.74	15.36	490.2	554.7	0.730679	0.736498	0.731605
S420MC_90_3	1.78	15.19	496.2	556.7	0.810983	0.781704	0.762040
S420MC_90_4	1.87	15.43	487.1	553.7	0.868120	0.827642	0.797801
Average			490.6	554.3			0.768988

The resultatnt measurements can be seen in Tab. 4.1. Note that the measure-

ment of specimen S420MC_45_3 is not taken into account for the average value since there has very likely been some sort of a measurement error. In Fig. 4.4 we can see the engineering stress-strain curves of all the specimens subjected to the uniaxial tensile test. Note, that because the engineering curves assume the cross-sectional area to remain unchanged during the test, it is necessary to convert these stresses and strains to their *true* values in order to use them in the following FEA calculation.
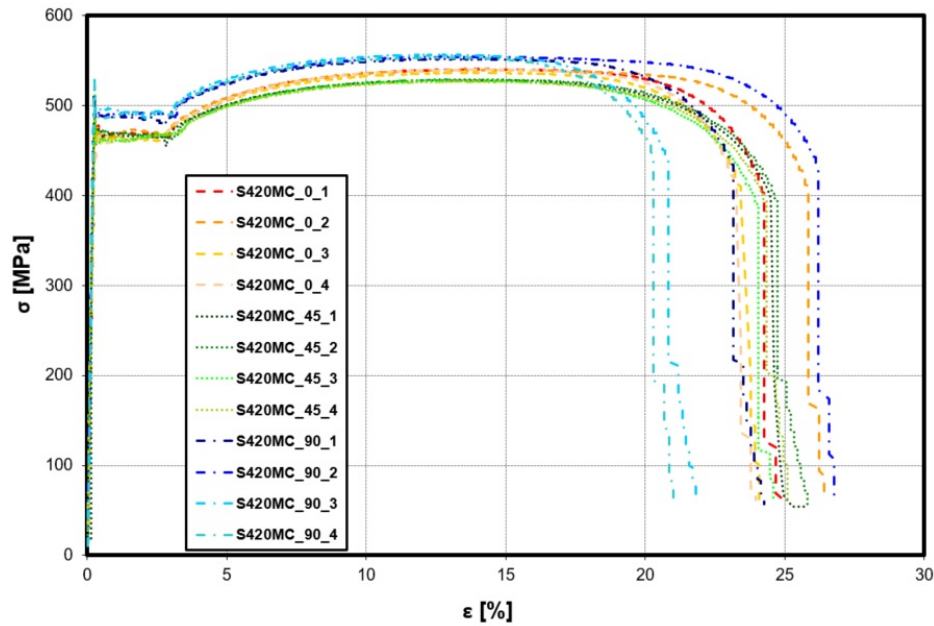

Figure 4.4: Engineering Stress-strain curves of uniaxial tensile tests.

Finally, the dependency of r-values on the angle towards rolling direction can be seen in Fig. 4.5
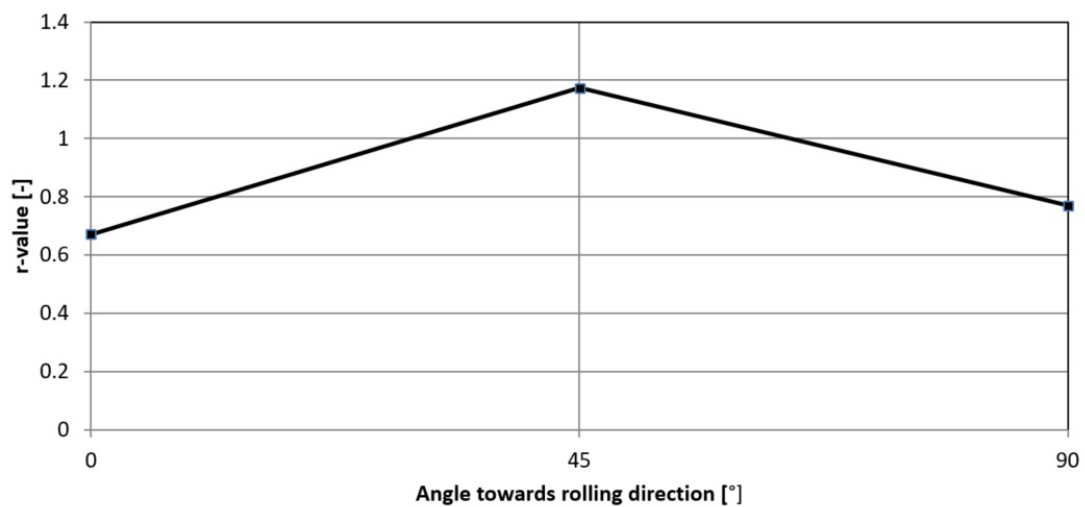

Figure 4.5: Dependency of r-values on the angle towards rolling direction.

4.1.2   Compression Testing

The stack tests were conducted also at room temperature of 23°C with a constant speed of 1 mm/min on a hydraulic press with a capacity of 400 kN (see Fig. 4.7). Once again, an optical measuring system that uses the DIC technique was used to obtain a precise deformation measurements. A pair of cameras was used; Camera 1 measured the deformation in the rolling direction (ϵ_1) and camera 2 measured the deformation in the transversal direction (ϵ_2). Moreover, the uniaxial deformation (in the direction of loading, ϵ_3) is also measured, see Fig. 4.6
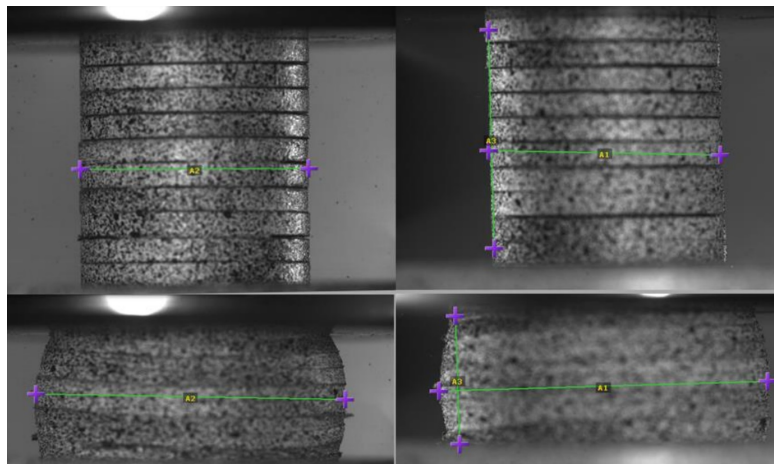

Figure 4.6: DIC of the stack test - Camera 1 (RD) on the left, Camera 2 (TD) on the right. [Comtes]
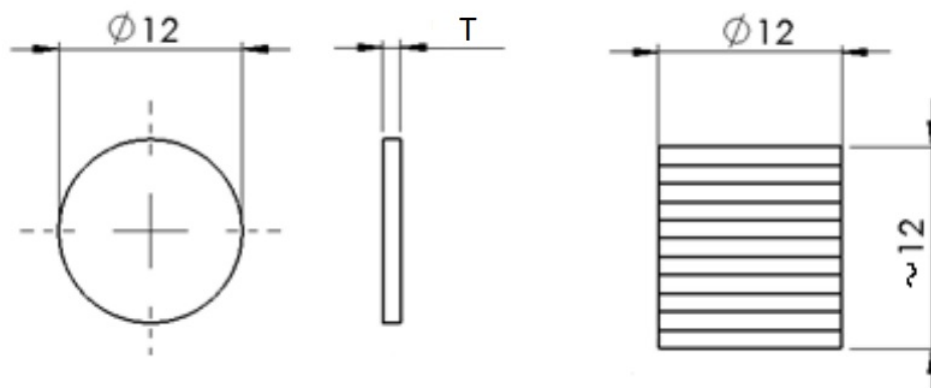
The specimen geometry can be seen in Fig. 4.7

Figure 4.7: Stack test specimen geometry.[Comtes]

It can be seen that multiple specimens were used in such a way, that the ratio of the diameter and stack height is as close to 1 as possible. In order to minimize

a phenomenon called *barrelling*, special polished jaws with a friction coefficient < 0.05 were used. The setup is shown in Fig. 4.8.
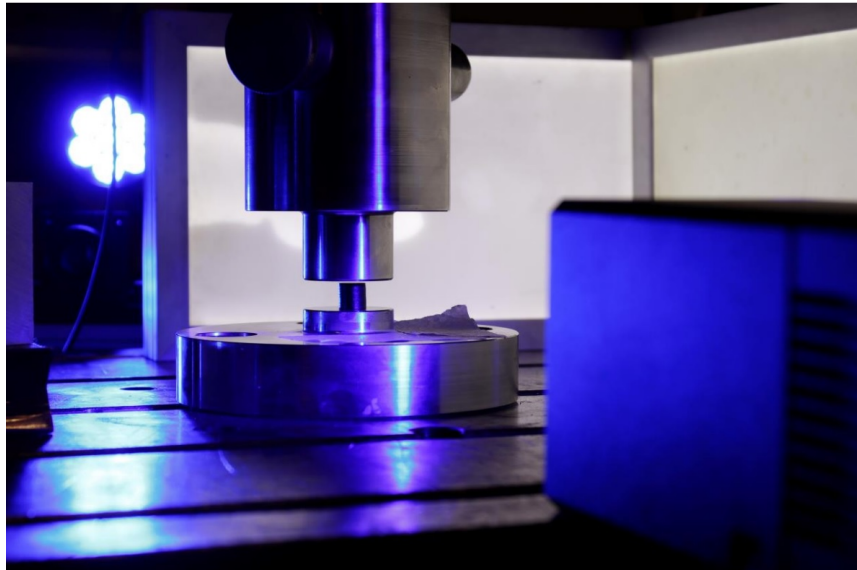

Figure 4.8: Stack test setup.[Comtes]

Finally, the true stress-strain curve can be seen in Fig. 4.9. Note that true strain in the normal direction ϵ_3^{true} is shown in this figure.
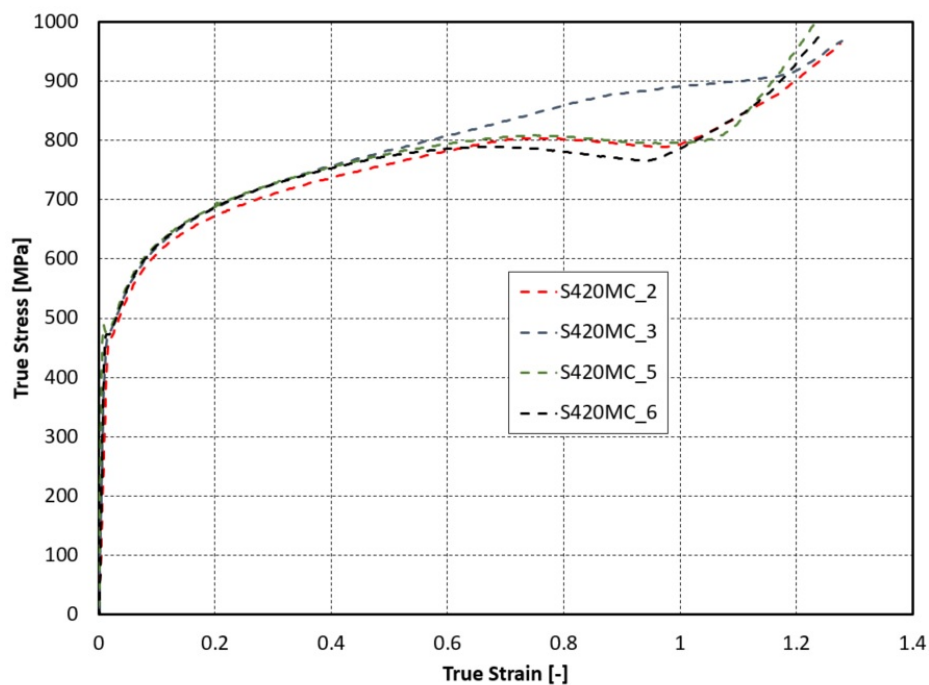

Figure 4.9: True stress-strain curves of the stack tests.

4.2   ANSYS Inputs

To create a material model in Ansys Workbench, we need to specify certain material properties. Those can be seen in Tab. 4.2

Table 4.2: Elastic material properties.

ρ	E	ν
kgm^{-3}	MPa	-
7850	$2 \cdot 10^5$	0.3

As mentioned in the end of Chapter 3, it is necessary to calculate the yield stress ratios. We can easily get the constants F, G, H and N from the experimentally determined r-values. Plugging in equations 3.80 through 3.83, we can solve for the yield stress ratios. Those will be used as a starting point for our material model. Taking the average values from Tab. 4.1 gives following values

Table 4.3: Experimental constants.

F	0.52244
G	0.59825
H	0.40175
N	1.87527

and solving for the yield stress ratios gives

Table 4.4: Yield stress ratios

R_{xx}	1
R_{yy}	1.04021
R_{zz}	0.94462
R_{xy}	0.89436

The last necessary input is a hardening plasticity model. In this case we use the multilinear isotropic hardening model. It uses a piecewise linear function to capture the nonlinear strain hardening response up until necking begins (note it does not support a curve with a negative slope, hence it cannot capture necking). It is defined by plastic strain vs. true stress σ_{true} given by

$$\sigma_{true} = \sigma_{eng}(1 + \epsilon_{eng}). \tag{4.1}$$

In other words, the starting point is defined as $(0, \sigma_y)$. This input is based on the experimental data from the uniaxial tensile test in rolling direction and can be seen in Fig. 4.10
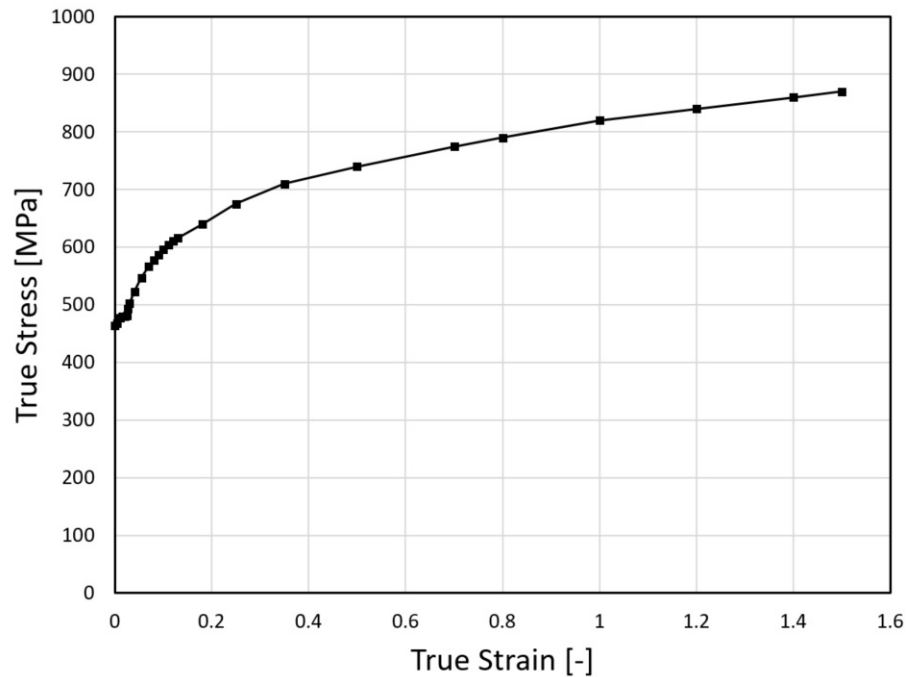
Figure 4.10: Multilinear hardening model.

Note that the stack test data were not used to prepare the material model, but are used later to confirm its validity.

4.3   Uniaxial Tensile Test Simulation

In this section we verify that our material model fits the experimental data by performing a simulation of both the uniaxial tensile and compression stack tests. In the first simulation, yield stress ratios from the previous section were used as a starting point. Those were then adjusted to get as good of a fit as possible.

4.3.1   Mesh

Due to the simple geometry of the test specimen, best convergence is achieved with a Hex Dominant Method. A mesh with 3418 elements and 16634 nodes was sufficiently fine to get accurate enough results. It can be seen in Fig. 4.11.
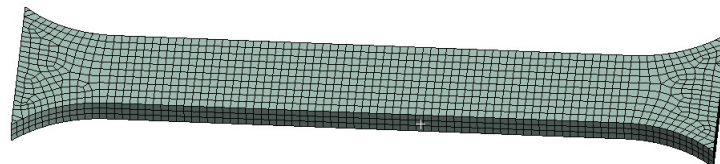

Figure 4.11: Mesh of the specimen.

4.3.2   Boundary conditions

Since both ends of the specimen are assumed to be rigid, there is no need to model them and instead a fixed support on one end and an applied force on the other was used to drive the deformation (see Fig. 4.12).
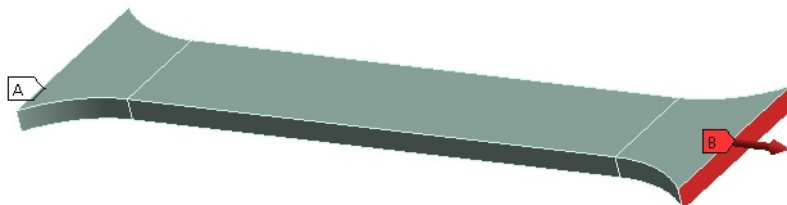

Figure 4.12: Boundary conditions.

The forces taken for the simulation are similar to the measured forces at breaking point of the specimen and can be seen in Tab. 4.5.

Table 4.5: Forces used for different directions.

F_0	F_{45}	F_{90}
N	N	N
43000	40000	44000

In order to get enough data points for an accurate evaluation, it is also important to configure the time steps (note that this simulation is time independent, time merely serves as a parameter). Those were chosen as follows:

- Initial time step $= 1 \cdot 10^{-2}$ s

- Minimum time step $= 1 \cdot 10^{-3}$ s

- Maximum time step $= 5 \cdot 10^{-2}$ s

and the entire simulation is done in one load step (given as 1s). The first results can be seen in Fig. 4.13. It is clearly visible that both simulations in rolling and transversal directions fit nearly perfectly, but the curve for the 45° offset direction yields much sooner.
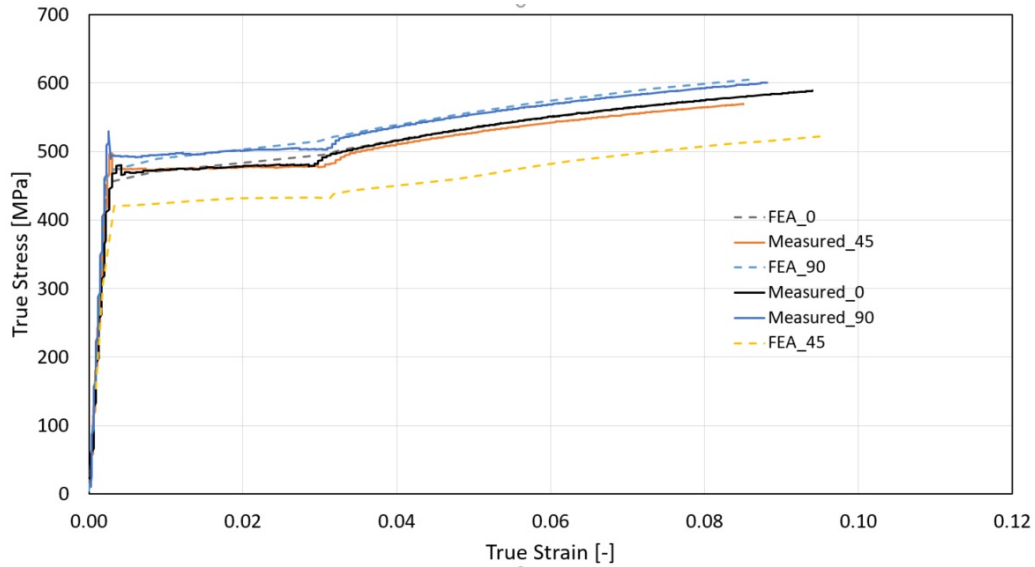
Figure 4.13: Comparison of measured and simulated results.

In order to resolve this issue, we can specify the yield stress ratio directly by using the average values from Tab. 4.1, rather than using the r-values. Doing so gives $R_{xy} = 1.01012$. After running the simulation again using this value, all the curves coincide with the measured data almost perfectly (see Fig. 4.14).
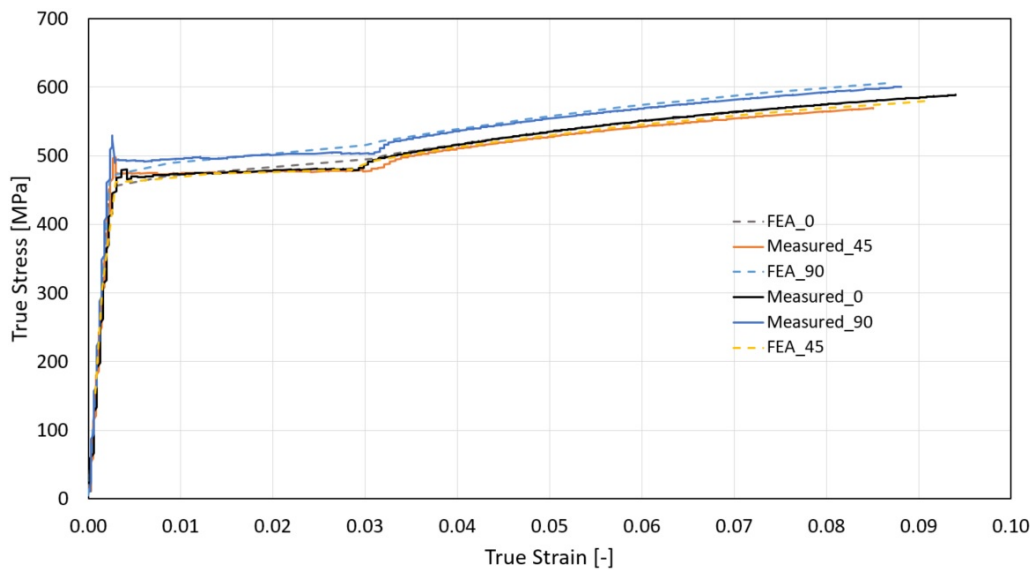

Figure 4.14: Comparison of experiment with the FEA calculation using adjusted values.

4.4   Stack Test Simulation

Now that the yield stress ratios have been adjusted to best fit the experimental data, we can also perform a stack test simulation. Thanks to the radial symmetry

of the specimens, we can use a quarter model to save calculation time.

4.4.1   Mesh

A mesh with 25443 nodes and 4882 elements was sufficient for this calculation (see Fig. 4.15).
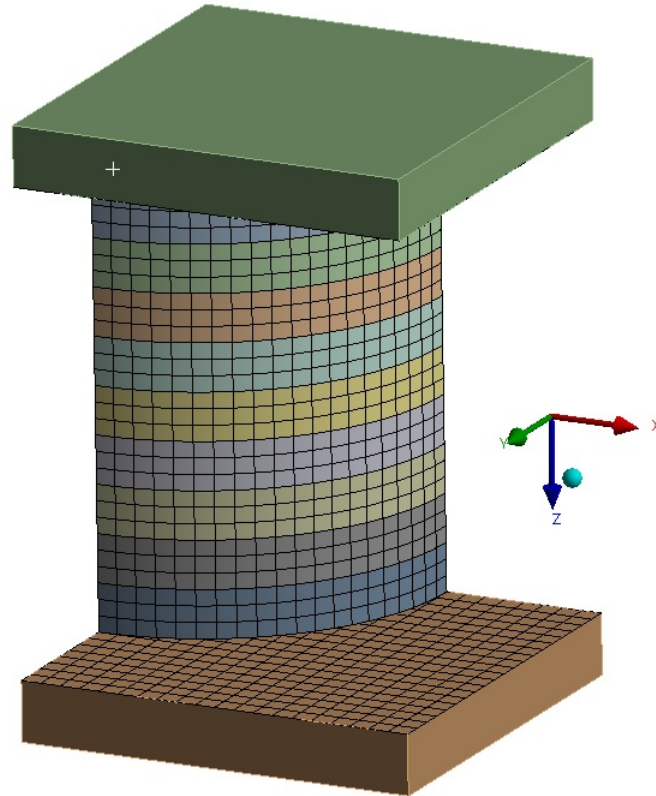

Figure 4.15: Mesh of the stack test model.

4.4.2   Boundary conditions

The jaws of the hydraulic cylinder were modeled as rigid bodies. The friction coefficient μ between the jaws and specimens was set as specified to $\mu_{jaws} = 0.05$ and to $\mu_{cylinders} = 0.15$ in the contact regions between each specimen. The deformation is driven by setting the displacement of one jaw to zero and using a remote displacement boundary condition on the other. It is also necessary to account for symmetries. This is done by setting displacements to zero normal to the faces that result from a cut by a plane of symmetry. This can be seen in Fig. 4.16.
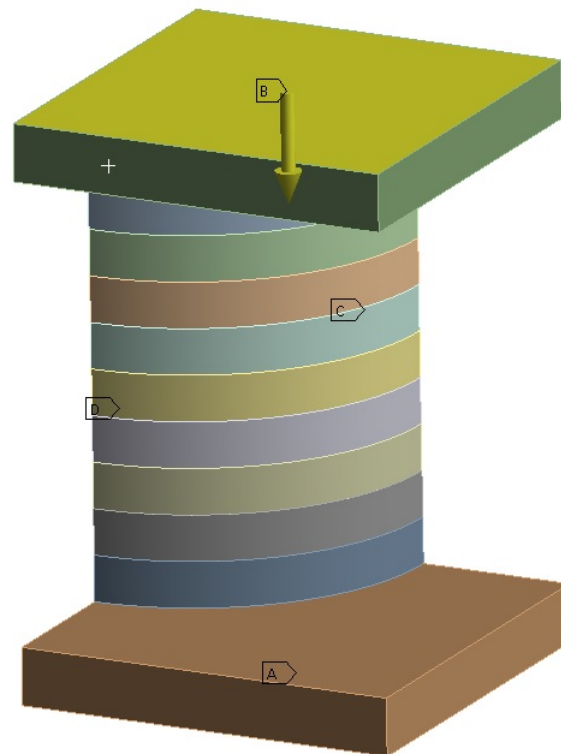
Figure 4.16: Boundary conditions of the stack test model.

A comparison of results of this simulation can be seen in Fig. 4.17;stress distribution in rolling direction (Fig. 4.17(a)) and transversal direction (Fig. 4.17(b)). We can also see the barrelling effect that is does coincide with the experiment.
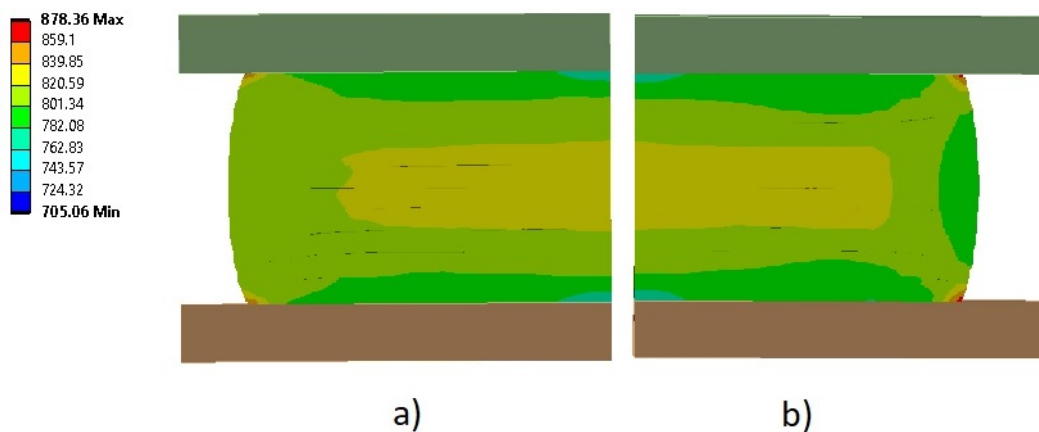

Figure 4.17: Total deformation result of the simulation with visible barrelling effect.

Finally in Fig. 4.18 we can see comparison of the true stress-strain curves. It is clear that the fit is reasonably good, which firther confirms the validity of material model chosen.
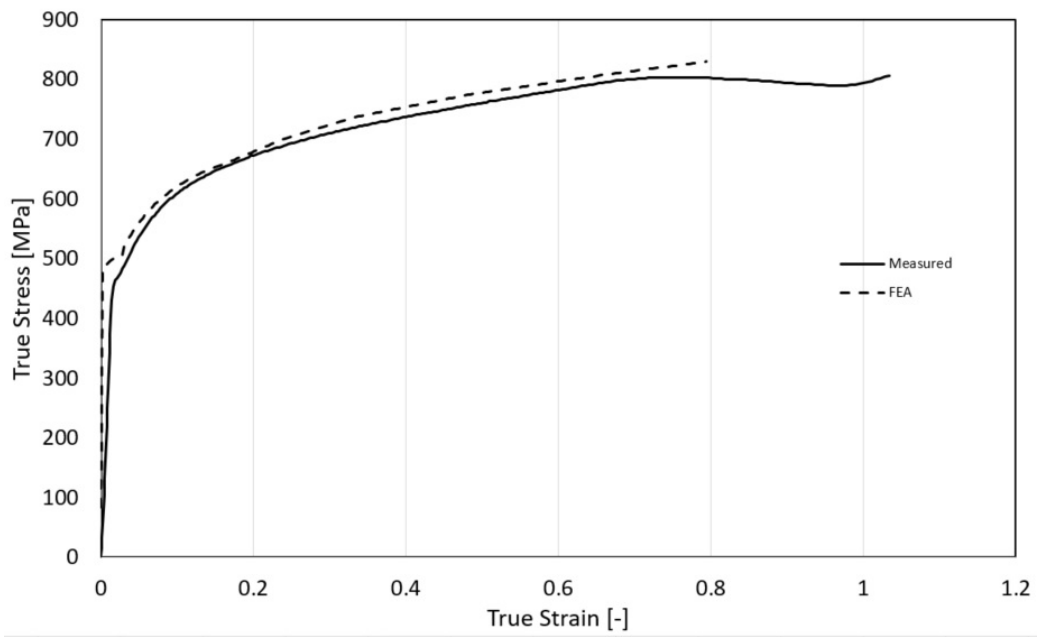
Figure 4.18: Comparison of measured and simulated results.

Chapter 5

Simulations

In this chapter, we focus on the setup and results of the simulations. Both isotropic and anisotropic cases will be assumed and results of both will be compared.

5.1 Anti-roll Bar

The anti-roll bar (or sway bar, see Fig. 5.1) is a device, usually a torsion spring, that helps to reduce body roll of a vehicle during fast cornering or over road irregularities.
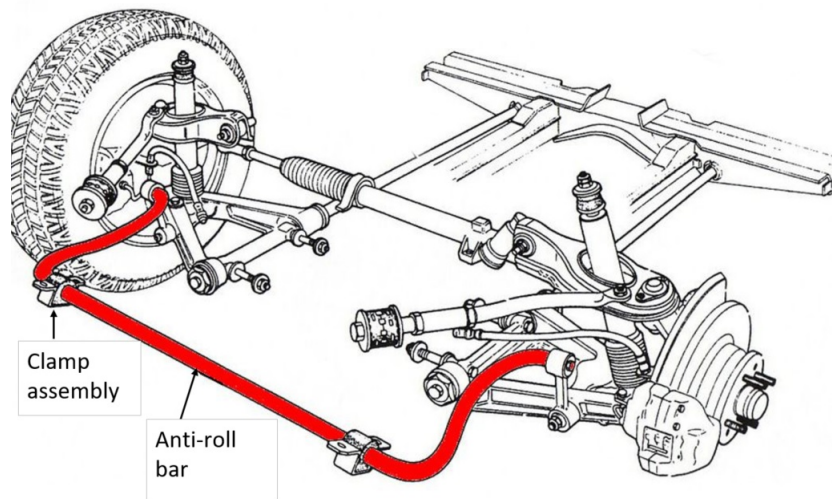

Figure 5.1: Anti-roll bar schematic.[22]

There are two main functions to the anti-roll bar:

- Reduction of body lean.

- Tuning of vehicle understeer/oversteer by changing the proportion of the total roll stiffness that comes from the front and rear axles.

It is held in place by two clamps with a rubber bearing as shown in Fig. 5.2. It is the aim of this thesis to determine whether the anisotropic properties of sheet metals do have significant influence on fatigue life of these clamps. In order to do that, it is first necessary to determine the plastic strains resulting from the forming operations. Secondly, we need to know the stresses that arise from the pressed-in rubber bearing, as well as the stresses that arise due to the loading of the anti-roll bar.

Figure 5.2: Clamp with rubber bearing (testing assembly for fatigue life evaluation).

5.2   Forming simulation

Firstly, we will focus on the forming operation. It consists of two steps and the entire process can be seen in Fig. 5.3
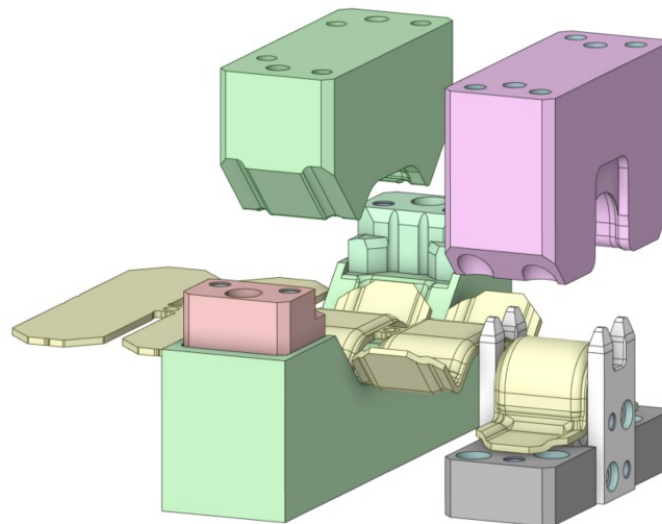

Figure 5.3: CAD model of the forming process.

The geometry of both the clamp and forming tools is quite complex, but due to

the fact that the clamp is symmetrical with respect to two perpendicular planes, it is sufficient to only model one quarter of it. The used model of the entire process and just the metal sheet strip is shown in Fig. 5.4
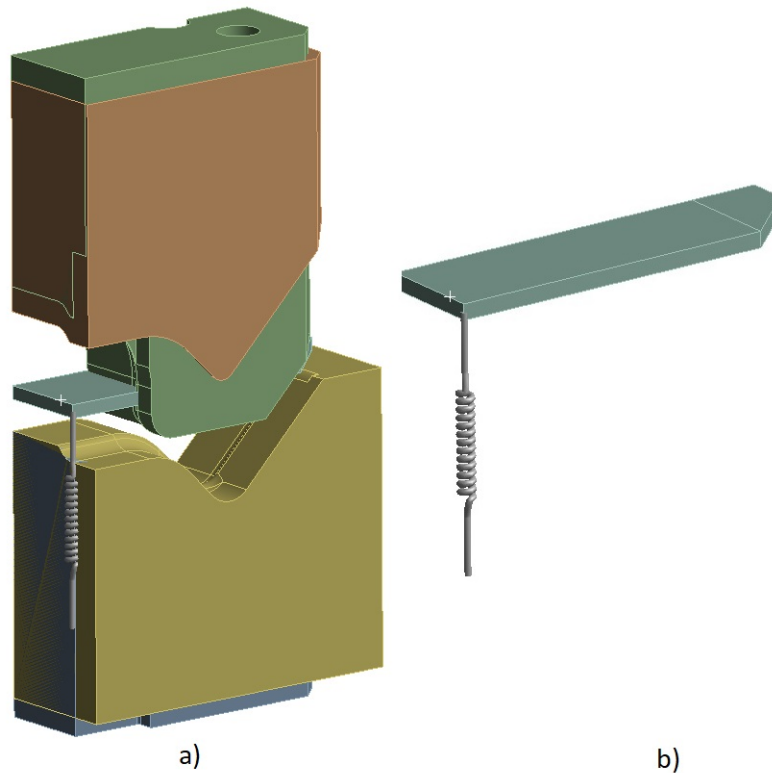

Figure 5.4: Quarter models - a) Entire quarter model b) Metal sheet strip.

5.2.1   Mesh

All the forming tools were modelled as rigid, which allows us to only mesh the forming surfaces rather than entire tools. For these surfaces, linear hexahedral and pentahedral elements of size 1 mm were used. In order to get accurate results, a fine mesh needed to be used for the metal sheet strip. The resultant mesh consisted of 40535 nodes and 36143 elements.
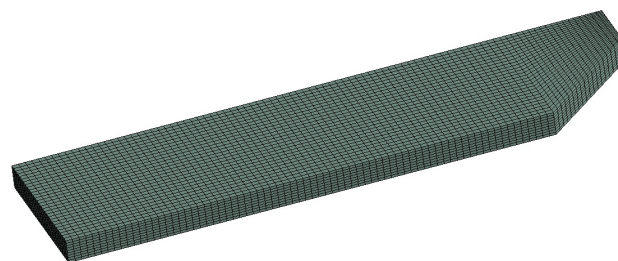

Figure 5.5: Mesh of the sheet metal strip.

5.2.2   Contact Regions

It is necessary to define a type of each contact region. In this case, all of the contacts are assumed frictional with a friction coefficient $\mu = 0.05$. However, since both of the forming operations are simulated in one calculation, we need to specify when certain contact regions are active and inactive. In this case it's rather simple. The first operation is simulated in the first time step, so the contact regions between the first set of tools and the strip are active, the rest is inactive. When the first operation is complete, these first contact regions become inactive and the second set of contacts activates. In order to see springback, the second set becomes inactive in the very last time step.
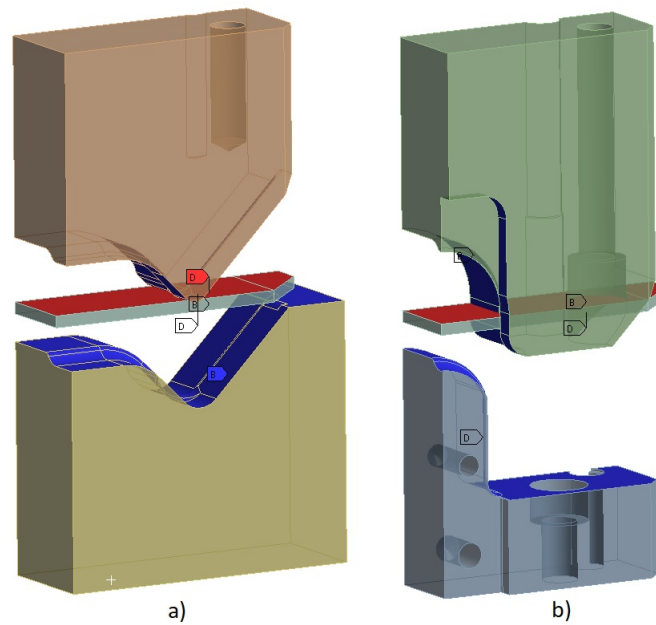
Figure 5.6: Contact regions - a) First set, b) Second set

5.2.3   Boundary Conditions

Since we used a quarter model due to symmetry, we need to define those symmetries in boundary conditions. We can do that simply by putting the displacement equal to zero in a direction perpendicular to a face that results from a cut by the plane of symmetry. For example, since we assume the X axis to coincide with the rolling direction, in the case where the long side of the strip is in the rolling direction, the longitudinal symmetry is along the X axis, or $u_x = 0$ and u_y, u_z are free.

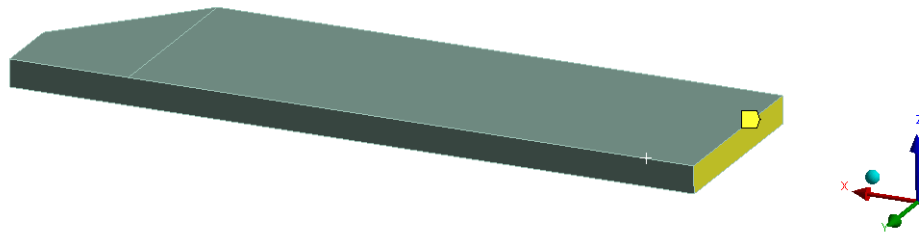Figure 5.7: Longitudinal symmetry in the 0°case.

The same is defined for the transversal symmetry along the Y axis. In Fig. 5.4, we can see a spring element attached to the strip. This element is necessary to prevent the model from "flying" away as the first contact between the tool and the strip happens. Lastly, we need to define the movement of the forming tools. We keep one of the tools fixed in place and define a displacement in the normal direction to the strip u_z equal to the desired movement of the tool in the particular operation (see Fig. 5.8). It is also important to to set all the other displacements $u_x, u_y, \phi_x, \phi_y, \phi_z$ equal to zero.

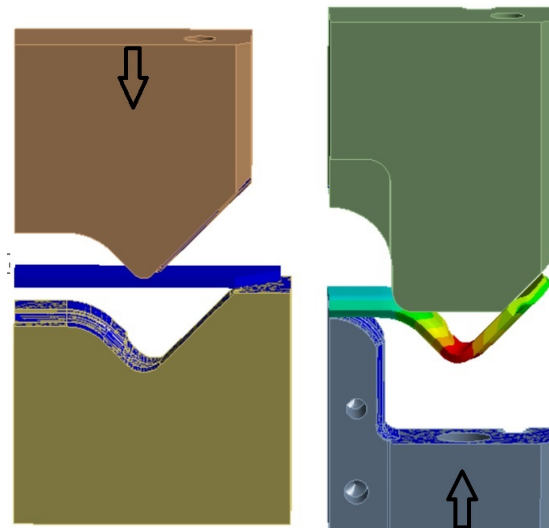Figure 5.8: A model of both forming operations.

5.2.4   Results

Plastic strain

The most important result which serves as an input for the following fatigue life evaluation is effective plastic strain, since we can then determine hardening effects. The results for an isotropic material and then anisotropic material in 0°, 45° and 90° with respect to rolling direction, respectively, can be seen in Fig. 5.9.
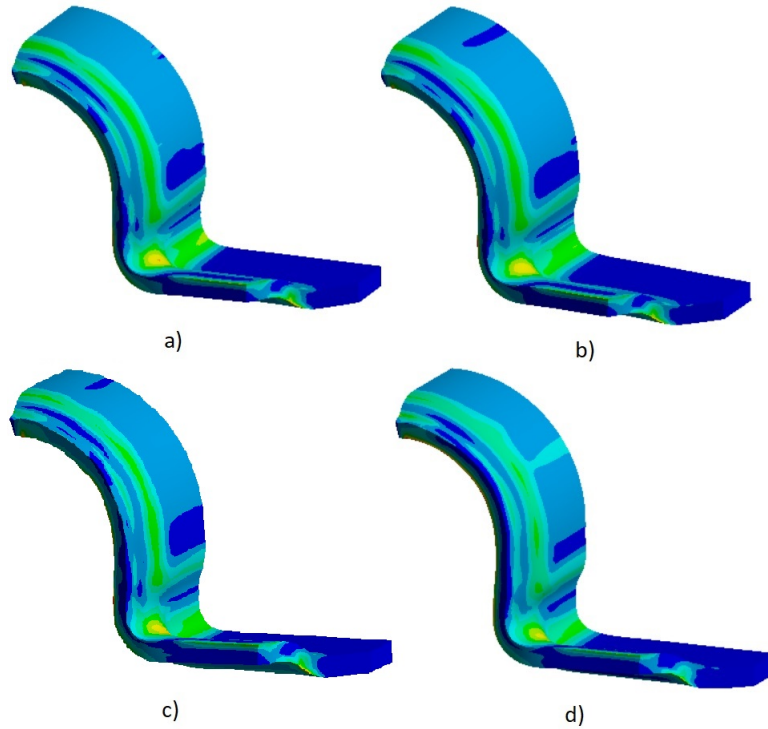
Figure 5.9: Equivalent plastic strain for - a) isotropic material b) anisotrpic material in 0° w.r.t RD, c) 45° w.r.t. RD and d) 90°w.r.t. RD.

Equivalent Stress

In this part we focus on the residual stresses after forming. However, these will not be used as an input for the fatigue life simulation, as the residual stress relaxes during cyclic loading and there are no data to capture its effect accurately. The first simulation assumed isotropic behaviour of the sheet metal. The multilinear hardening model used is the same as for the following anisotropic simulation and Ansys uses the von Mises theory for plasticty, so a yield criterion in a form

$$F = \left[\frac{3}{2} \{s\}^T [M] \{s\} \right]^{\frac{1}{2}} - \sigma_k = 0 \tag{5.1}$$

where σ_k is the yield stress and is a function of the amount of plastic work done is used [21]. In Fig. 5.10 we can see a comparison of the equivalent stress at the end of the second operation (a) and after springback (b) for the isotropic case. Note that the maximum occurs in an area that is of no particular interest. We know from the experimental tests that failure almost always occurs in the area shown in Fig. 5.11. If we increase the number of elements, this maximum value seems to continue to rise. That might likely be a result of shear locking, which occurs in first-order fully-integrated elements that are subjected to bending, or volumetric locking is a result of the underlying assumption that plastic deformation is isochoric.

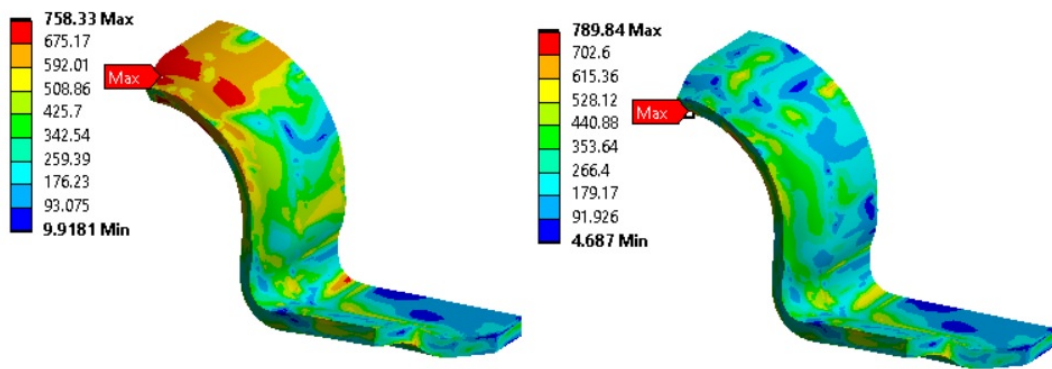Figure 5.10: Equivalent stress after forming assuming isotropic behaviour - a) Before springback b) After springback

Figure 5.11: Clamp fracture due to fatigue.

The results accounting for the anisotropic behaviour at 0°, 45°and 90°, respectively, can be seen in figures 5.12, 5.13 and 5.14.
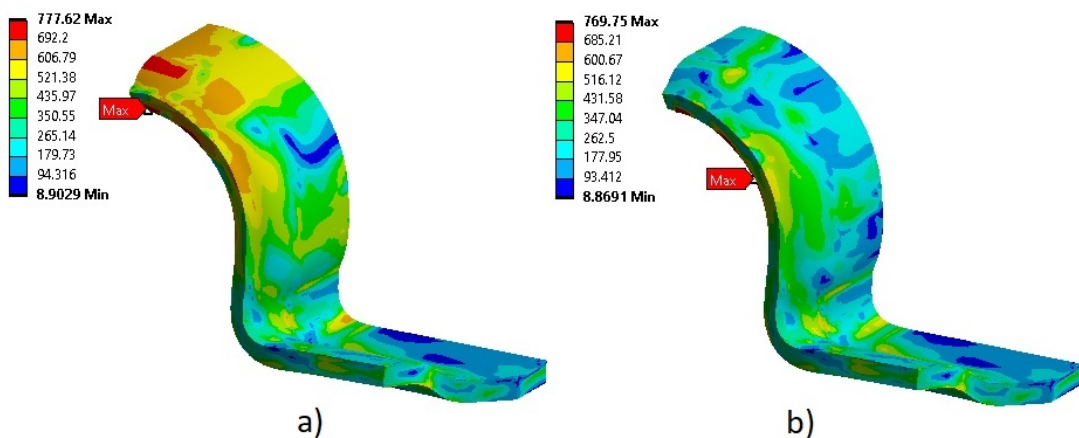
Figure 5.12: Equivalent stress after forming at 0° w.r.t. RD - a) Before springback b) After springback

It is clear that anisotropy has a significant impact on the residual stresses after forming. The highest stress values were reached in the case of transversal direction. However, after springback, this case has the lowest residual stresses in the problematic area.
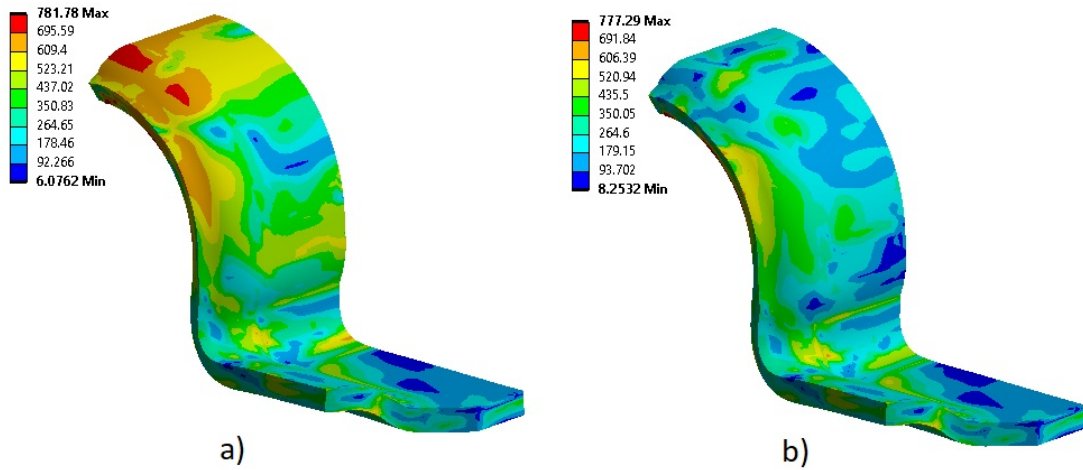
Figure 5.13: Equivalent stress after forming at 45° w.r.t. RD - a) Before springback b) After springback
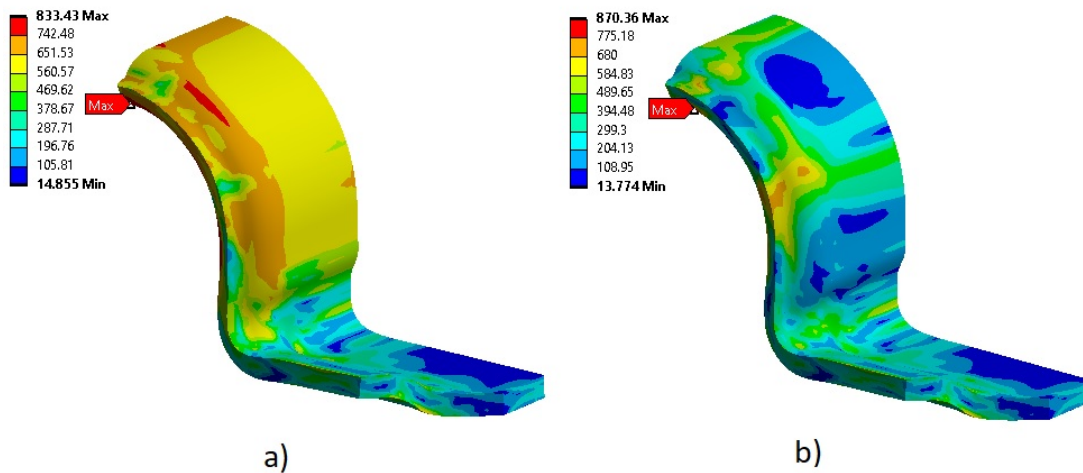

Figure 5.14: Equivalent stress after forming at 90° w.r.t. RD - a) Before springback b) After springback

5.3   Rubber bearing press fit

In the previous section, we have determined the plastic deformation and the residual stresses after forming in various directions. Now we need to determine the stresses resulting from one load cycle. To do that, we must first find a suitable

material model for the elastomer the rubber bearing is made of and then use it to determine how the loads acting on the anti-roll bar transfer through this bearing onto the clamp. Since this material is assumed to be hyperelastic, we can choose from various models. Unfortunately, there are very few measurements to base our material model on. However, for our purposes it is sufficient to only have a vague approximation of how this press-fit affects the clamp. The material model used will be chosen to best fit a hysteresis loop of the entire bar-bearing-clamp assembly, which has been determined experimentally.

5.3.1   Mooney-Rivlin 3 Parameter Model

The Mooney-Rivlin model is a special case of the generalized Rivlin model (also called the polynomial hyperelastic model) which has the form

$$W = \sum_{p,q=0}^{N} C_{pq}(\bar{I}_1 - 3)^p(\bar{I}_2 - 3)^q + \sum_{m=1}^{M} \frac{1}{D_m}(J - 1)^{2m}. \qquad (5.2)$$

Here, C_{pq} are material constants related to the distortional response and D_m are material constants related to the volumetric response. In our case, we use the three-parameter Mooney-Rivlin model that can be used in Ansys. Equation 5.2 reduces to

$$W = C_{10}(\bar{I}_1 - 3) + C_{01}(\bar{I}_2 - 3) + C_{11}(\bar{I}_1 - 3)(\bar{I}_2 - 3) + \frac{1}{d}(J - 1)^2 \qquad (5.3)$$

where d is known as the incompressibility parameter. The parameters chosen for this model can be seen in Tab. 5.1.

C_{10}	C_{01}	C_{11}	d
MPa	MPa	MPa	MPa^{-1}
55	-20	-5	0.1

Table 5.1: Coefficients for the Mooney-Rivlin model.

5.3.2   Model

Since the only measured data related to the rubber bearing are the hysteresis measurements, they are used as the ground to find a reasonable approximation of its behaviour for the simulation. The anti-roll bar with the bearing is first pressed into the clamp and subsequently a plate presses the rubber further in. Then a force is applied to the anti-roll bar.

5.3.3   Mesh

A mesh with 53466 nodes and 25116 elements was sufficient for this calculation.
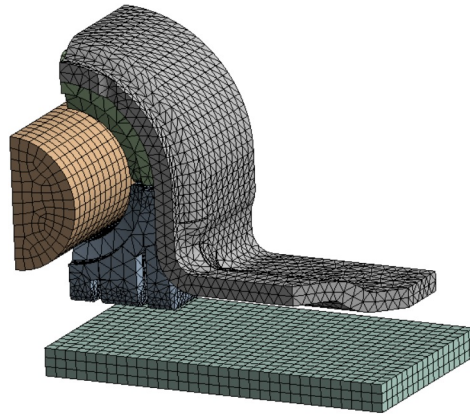
Figure 5.15: Mesh of the assembly.

5.3.4   Boundary Conditions

The clamp is fixed in place by two screws. We can approximate this by using a fixed support at the area the washer would cover. Zero displacements on the faces against which the clamp is symmetrical are also applied. The rubber bearing is pressed in and the bottom plate then moves up. After that a force is applied to the anti-roll bar ranging from 0 to 5000 N both in the positive and negative normal direction. It is clear that the hysteresis loop is mostly overlapping with the experimental results, which confirms that the chosen material model is a good approximation of reality.

5.3.5   Results
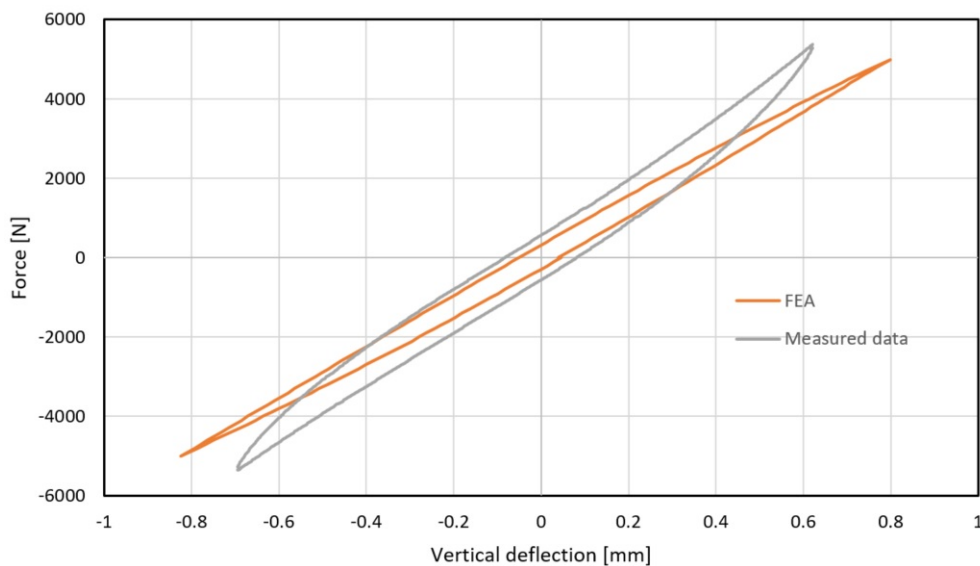
Figure 5.16: Hysteresis loop - experiment and FEA comparison.

It can be seen in Fig. 5.16 that the material model chosen for the rubber bearing fits the hysteresis data quite well. The displacement coming from a simulation behaves more linearly than reality, which is likely caused by a relatively simple material model used in combination with a fact that the rubber bearing also has an aluminium ring pressed into it, which would be very difficult to simulate accurately.

Chapter 6

Fatigue life evaluation

The experiment had a force acting in the vertical direction, as seen in Fig. 6.1.

Figure 6.1: Force acting on the clamp.

Multiple tests were done with increasing forces. These are listed in Tab. 6.1

Table 6.1: Forces and frequencies.

Testing Force ±kN	Testing Frequency Hz
6	3
9	3
12	3
15	3
18	3

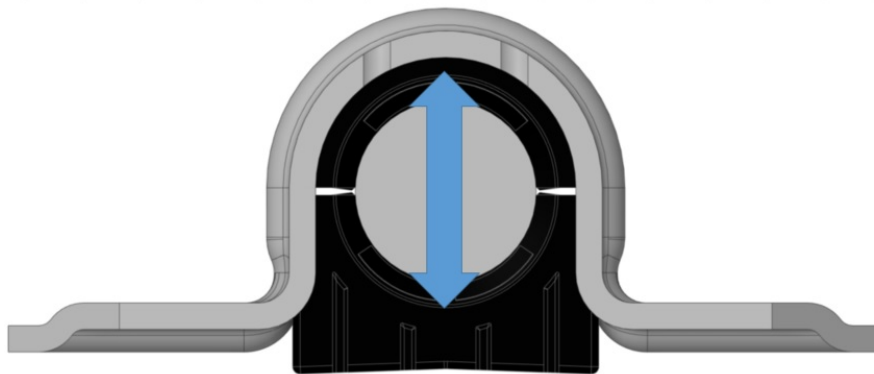The clamp is fixed in place by two M10x20 grade 10.9 screws and water was used as a lubricant. The whole testing setup is shown in Fig. 6.2
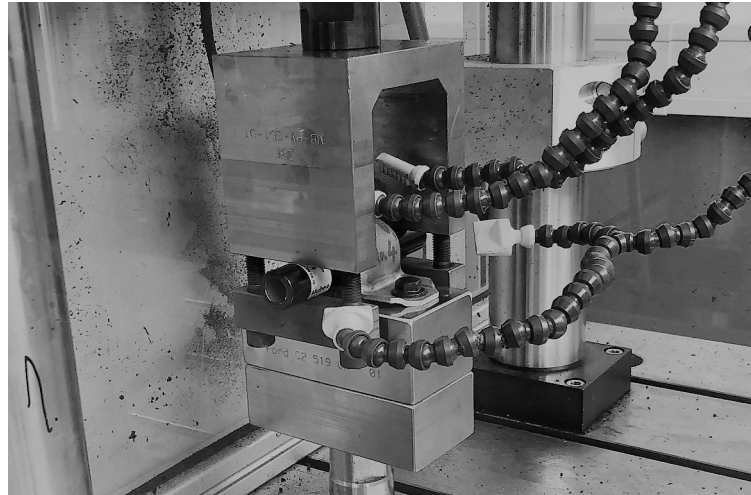
Figure 6.2: Testing setup.

6.1   Load cycle simulation

As mentioned before, we need to simulate one load cycle as an input for the fatigue life evaluation. To do that we use the same model as for the hysteresis simulation since the loading is in the same direction. Mesh of the clamp has also been refined and quadratic tetrahedral elements were used. The mesh can be seen in Fig. 6.3

Figure 6.3: Refined mesh with quadratic tetrahedral elements.

This simulation is performed assuming linear material behaviour, since FEMFAT software later corrects for material nonlinearities.

6.2   Result Mapping

This section concerns with a preparation of our final model for the fatigue life calculation. At this point, we have 2 inputs - plastic deformation as a result of forming and stress distribution as a result of loading. To use both, we need to map the results of the forming simulation onto the model that is used for loading simulation. To do that, we need to export the results of our forming simulation into a .csv file. We can then import the .csv files straight into ANSYS via an External Data module. It is also necessary to fit the data points, since the global coordinates usually differ. When the models sufficiently overlap, the plastics strain can finally be mapped from the linear hexahedral mesh onto the elements of the tetrahedral forming mesh, as shown in Fig. 6.4.
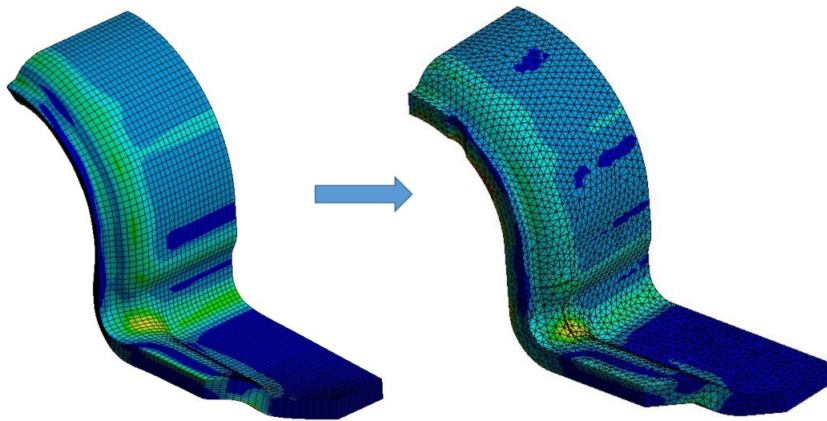
Figure 6.4: Example of a mapped result.

Lastly, a .erfh5 file with the mapped results is exported and will serve as one of the direct inputs into FEMFAT calculation.

6.3   FEMFAT Evaluation

6.3.1   FEMFAT

FEMFAT (Finite Element Method Fatigue) is a software for FEM based fatigue prediction. It utilizes a concept of transforming the material S-N curve from specimen tests into a local modified S-N curve for each node based on influence of different factors (such as stress condition, material properties, surface roughness, local plasticity, etc...).

6.3.2   Results

The overview of all simulation results can be seen in Tab. 6.2, where N_f stands for number of cycles until failure and ESF for endurance safety factor.

Table 6.2: Fatigue life calculation results.

Force $\pm$kN	N_f	ESF
Isotropic		
6	$1 \cdot 10^8$	1.3222
9	$4.2 \cdot 10^7$	1.2146
12	$2.97 \cdot 10^5$	0.9412
15	77754	0.7434
18	36190	0.6134
0° w.r.t RD		
6	$1 \cdot 10^8$	1.3303
9	$4.8 \cdot 10^7$	1.2226
12	$3.1 \cdot 10^5$	0.9454
15	79618	0.7465
18	36896	0.6159
45° w.r.t RD		
6	$1 \cdot 10^8$	1.3312
9	$4.5 \cdot 10^7$	1.2264
12	$3.1 \cdot 10^5$	0.9437
15	78883	0.7459
18	36601	0.6149
90° w.r.t RD		
6	$1 \cdot 10^8$	1.3096
9	$2.5 \cdot 10^7$	1.2264
12	$3.6 \cdot 10^5$	0.9212
15	69281	0.7332
18	32298	0.6033

Averaged experimental results can for comparison be seen in Tab. 6.3

Table 6.3: Averaged experimental results

Force $\pm$kN	N_{fexp}
6	$2 \cdot 10^6$
9	$2 \cdot 10^6$
12	1273711
15	199153
18	109872

Finally, visualization of the ESF result is shown in fig 6.5.
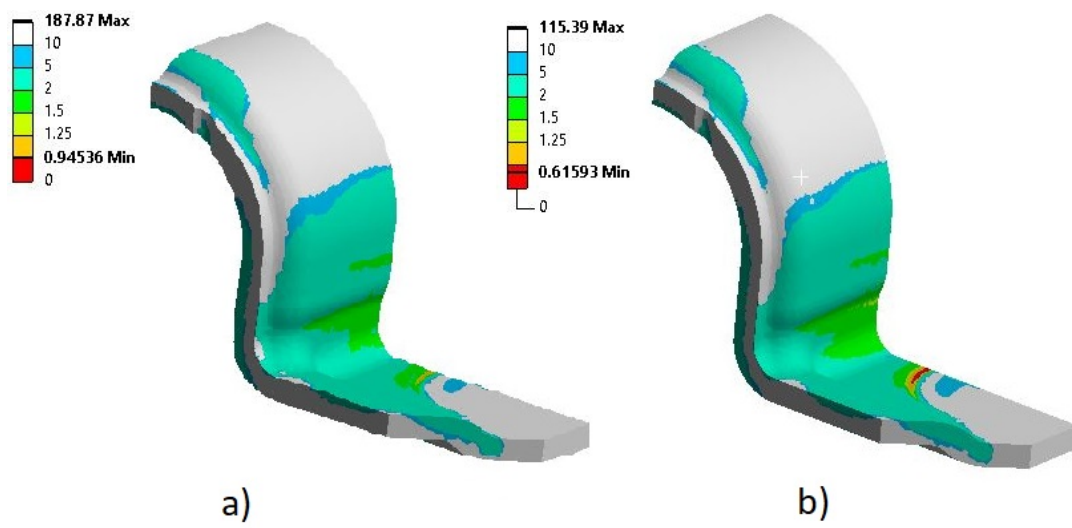

Figure 6.5: Visualization of the ESF result - a) 0°, 12kN b) 0°, 18kN.

Chapter 7

Conclusions

The goal of this thesis was to evaluate the influence anisotropic behaviour of sheet metal has on plastic straining and hardening that arise during forming processes. This knowledge was later used to estimate fatigue life of a part made of a given sheet metal.

The first part of this thesis gave a brief overview of the theory of linear elasticity, anisotropic elasticity and also shown their application to sheet metal modelling. Basics of the theory of plasticity were introduced next; isotropic yield criteria, hardening rules, flow rule and finally Hill's 1948 yield criterion.

In the second part, anisotropic material model for the S420MC steel was proposed based on the experimental measurements. This model was then validated by performing finite element simulations of uniaxial tensile tests in rolling direction, transversal direction and 45° direction with respect to rolling direction, which shown a good agreement between the experiment and simulation.

Having the anisotropic material model ready, simulation of a forming process was performed. This shown that anisotropy indeed has a significant influence especially on residual stresses, but also on plastic straining.

Function of the anti-roll bar and a way it is held in place was then briefly explained. Since it was the aim to later determine fatigue life of the clamp, it was necessary to simulate its loading through the whole assembly. That meant a need to create a hyperelastic material model to capture the behaviour of a rubber bearing through which loads are applied on the clamp. This was done using Mooney-Rivlin 3 parameter model that is available in ANSYS Workbench and using hysteresis measurements of the assembly to fit onto. This bearing also has an aluminium ring pressed into it and generally its behaviour is quite complex, which meant the model used in the simulation was only a vague approximation of reality.

Plastic strains that resulted from forming were then mapped onto the clamp model used for loading simulation. This ensured that hardening which occurs during forming was included. The same model used for hysteresis calculation was used to perform one load cycle for various forces ranging from 6 to 18 kN. These results were finally evaluated by FEMFAT software, which gave an estimate of cycles to failure and the endurance safety factor. It is clear that anisotropy does

have an impact on fatigue life of this clamp, especially for lower force ranges. However, there was a disagreement with the experiment. The simulation results were suggesting that failure occurs much earlier than in reality. This can likely be a result of an inaccurate material model of the elastomer bearing and it would be the main goal to create a more suitable one in order to get more precise results in the future.

Bibliography

[1] MARCINIAK, Z., J. L. DUNCAN, S. J. HU. *Mechanics of sheet metal forming.* Oxford: Butterwort-Heinemann, 2002. ISBN 0-7506-5300-0.

[2] BANABIC, D. *Sheet metal forming processes: constitutive modelling and numerical simulation.* 2010th edition. New York: Springer, 2010. ISBN 3540881123.

[3] Constitutive Equations. Massachusetts Institute of Technology [online]. Cambridge (Massachuttes): MIT, 2013 [cit. 2022-08-10]. Available at: `http://web.mit.edu/16.20/homepage/3_Constitutive/Constitutive_files/module_3_with_sosolutio.pdf`

[4] HILL, Rodney. *The mathematical theory of plasticity.* 2nd edition. Oxford: Oxford University Press, 1998. ISBN 0198503679.

[5] TANG, Sing C., J. PAN. *Mechanics modeling of sheet metal forming.* Warrendale, Pa.: SAE International, 2007. ISBN 0768008964.

[6] Tresca H (1864) On the yield of solids at high pressures. Comptes Rendus Academie des Sciences (in French)

[7] SWANBOM,M. [TheBom_PE]. (2018, 9 January). Distortion Energy Static Failure Criterion; Von Mises Stress [Video]. YouTube. `https://www.youtube.com/watch?v=C_OBIN7oj_4`

[8] CHEN, Wai-Fah, D. J. HAN. *Plasticity for structural engineers.* Ft. Lauderdale, FL: J. Ross Pub., 2007. ISBN 9781932159752.

[9] *Introduction to Plasticity* [online]. In: . [cit. 2022-08-12]. Available at: `https://pkel015.connect.amazon.auckland.ac.nz/SolidMechanicsBooks/Part_II/08_Plasticity/08_Plasticity_Complete.pdf`

[10] von Mises RV (1928) Mechanics of plastic deformation of crystals. Zeitschrift für Angewandte Mathematik und Mechanik (in German)

[11] KHAN, Akhtar a Sujian HUANG. *Continuum Theory of Plasticity.* New York: Wiley, 1995. ISBN 0471310433.

[12] HILL, Rodney. A theory of the yielding and plastic flow of anisotropic metals. *Proceedings of the Royal Society of London*, Series A, Vol. 193, 1948. Available at: `https://doi.org/10.1098/rspa.1948.0045`.

[13] HILL, Rodney. Theoretical plasticity of textured aggregates. *Mathematical Proceedings of the Cambridge Philosophical Society*, Vol. 85, 1979. Available at: `https://doi.org/10.1017/S0305004100055596`.

[14] HERSHEY, Allen. The Plasticity of an Isotropic Aggregate of Anisotropic Face-Centered Cubic Crystals. *Journal of Applied Mechanics*, Vol. 76, 1954. Available at: `https://doi.org/10.1115/1.4010900`.

[15] HOSFORD, William. A Generalized Isotropic Yield Criterion. *Journal of Applied Mechanics*, Vol. 69, 1972. Available at: `https://doi.org/10.1115/1.3422732`

[16] LOGAN, Roger and William HOSFORD. Upper-bound anisotropic yield locus calculations assuming ⟨111⟩-pencil glide. *International Journal of Mechanical Sciences*, Vol. 22, 1980. Available at: `https://doi.org/10.1016/0020-7403(80)90011-9`.

[17] KARAFILLIS, A.P., M.C. BOYCE. *A general anisotropic yield criterion using bounds and a transformation weighting tensor. Journal of the Mechanics and Physics of Solids* [online]. 1993, 41(12), 1859-1886 [cit. 2022-08-11]. ISSN 00225096. Available at: `https://doi.org/10.1016/0022-5096(93)90073-O`

[18] BARLAT, F., Y. MAEDA, K. CHUNG, *et al.* Yield function development for aluminium alloy sheets. *Journal of the Mechanics and Physics of Solids* [online]. 1997, 45(11-12), 1727-1763 [cit. 2022-08-11]. ISSN 00225096. Available at: `https://doi.org/10.1016/S0022-5096(97)00034-3`

[19] BARLAT, F., J.C. BREM, J.W. YOON, *et al.* Plane stress yield functions for aluminium alloy sheets - part 1: theory. *International Journal of Plasticity* [online]. 2003, 19(9), 1297-1319 [cit. 2022-08-11]. ISSN 07496419. Available at: `https://doi.org/10.1019/S0749-6419(02)00019-0`

[20] BARLAT, F., H. ARETZ, J.W. YOON, M.E. KARABIN, J.C. BREM, R.E. DICK. Linear transformation-based anisotropic yield functions. *International Journal of Plasticity* [online]. 2005, 21(5), 1009-1039 [cit. 2022-08-11]. ISSN 07496419. Available at: `https://doi.org/10.1016/j.ijpas.2004.06.004`

[21] ANSYS, Inc. (2020). *ANSYS Theory Reference*, ANSYS.

[22] ROBINSON, M. How do anti-roll bars actually work?. CarThrottle [online]. Cambridge (Massachuttes), 18 August 2018 [cit. 2022-08-10]. Available at: `https://www.carthrottle.com/post/how-do-anti-roll-bars-actually-work/`

[23] Von Mises yield criterion. In: *Wikipedia: the free encyclopedia* [online]. San Francisco (CA): Wikimedia Foundation, 2001- [cit. 2022-08-12]. Available at: `https://en.wikipedia.org/wiki/Von_Mises_yield_criterion`